

Advances in Optics and Photonics

Off-axis digital holographic multiplexing for rapid wavefront acquisition and processing

NATAN T. SHAKED,^{1,*} VICENTE MICÓ,² MACIEJ TRUSIAK,³ ARKADIUSZ KUŚ,³ AND SIMCHA K. MIRSKY¹

¹Department of Biomedical Engineering, Faculty of Engineering, Tel Aviv University, Tel Aviv 69978, Israel

²Department of Optics and Optometry and Vision Sciences, University of Valencia, C/Doctor Moliner 50, Burjassot 46100, Spain

³Warsaw University of Technology, Institute of Micromechanics and Photonics, 8 Sw. A. Boboli St., 02-525 Warsaw, Poland

*Corresponding author: nshaked@tau.ac.il

Received November 27, 2019; revised April 27, 2020; accepted May 27, 2020;
published August 10, 2020 (Doc. ID 384612)

Off-axis holographic multiplexing involves capturing several complex wavefronts, each encoded into off-axis holograms with different interference fringe orientations, simultaneously, with a single camera acquisition. Thus, the multiplexed off-axis hologram can capture several wavefronts at once, where each one encodes different information from the sample, using the same number of pixels typically required for acquiring a single conventional off-axis hologram encoding only one sample wavefront. This gives rise to many possible applications, with focus on acquisition of dynamic samples, with hundreds of scientific papers already published in the last decade. These include field-of-view multiplexing, depth-of-field multiplexing, angular perspective multiplexing for tomographic phase microscopy for 3-D refractive index imaging, multiple wavelength multiplexing for multiwavelength phase unwrapping or for spectroscopy, performing super-resolution holographic imaging with synthetic aperture with simultaneous acquisition, holographic imaging of ultrafast events by encoding different temporal events into the parallel channels using laser pulses, measuring the Jones matrix and the birefringence of the sample from a single multiplexed hologram, and measuring several fluorescent microscopy channels and quantitative phase profiles together, among others. Each of the multiplexing techniques opens new perspectives for applying holography to efficiently measure challenging biological and metrological samples. Furthermore, even if the multiplexing is done digitally, off-axis holographic multiplexing is useful for rapid processing of the wavefront, for holographic compression, and for visualization purposes. Although each of these applications typically requires a different optical system or processing, they all share the same theoretical background. We therefore review the theory, various optical systems, applications, and perspectives of the field of off-axis holographic multiplexing, with the goal of stimulating its further development. © 2020 Optical Society of America

<https://doi.org/10.1364/AOP.384612>

1. Introduction	558
2. Camera Spatial Bandwidth Considerations and the Multiplexing Limit . . .	562
3. Field of View Multiplexing	566
4. Depth-Of-Field Multiplexing and Displacement and Shape Measurements .	571
5. Wavelength Multiplexing	574
6. Multiplexing for Synthetic Aperture Super-Resolution	576
7. Angular Multiplexing for Tomography	584
8. Multiplexing Quantitative Phase Images with Fluorescence	588
9. Multiplexing Fast Events	591
10. Multiplexing for Polarization Measurements	591
11. Digital Multiplexing for Rapid Wavefront Retrieval	593
12. Conclusion and Perspectives	595
Funding	597
Disclosures	597
References	597

Off-axis digital holographic multiplexing for rapid wavefront acquisition and processing

NATAN T. SHAKED, VICENTE MICÓ, MACIEJ TRUSIAK,
ARKADIUSZ KUŚ, AND SIMCHA K. MIRSKY

1. INTRODUCTION

Holography can record the entire complex wavefront (amplitude and phase) of the light that interacted with a sample by recording interference between a beam that has interacted with the sample and a reference beam that does not contain the sample spatial modulation. From the recorded complex field, one can obtain the quantitative phase profile of the sample, which encodes both the sample physical thickness and refractive index profiles [1]. The applications of holography range from stain-free acquisition of biological cells *in vitro* to optical metrology and profiling of thin elements and chemical processes [1–11]. Holographic multiplexing means compression of additional information into the hologram, a preliminary idea proposed already in 1965 by Lohmann [12].

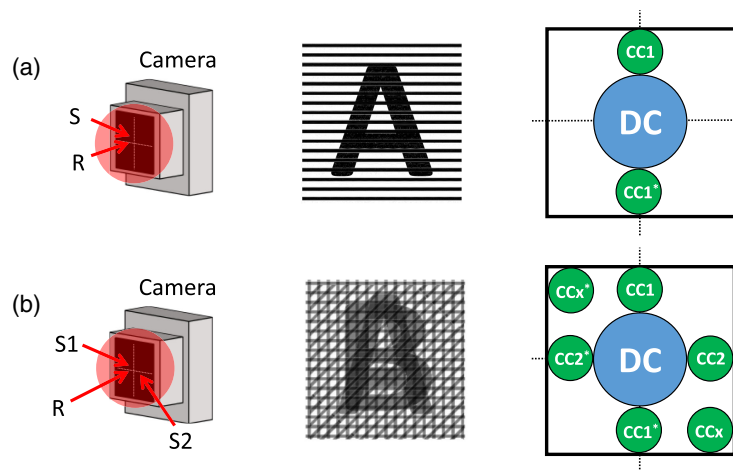
In general, there are two main approaches to holographic wavefront acquisition. In on-axis holography [13], the two beams interfere with no angle between them, producing a hologram that contains concentric circular interference fringes. This causes mixing of the sample and reference intensities with the complex wavefront of the sample. In the spatial frequency domain, the cross-correlation (CC) terms containing the sample complex wavefront spatial frequencies will overlap with each other as well as with the autocorrelation (DC) terms containing the spatial frequencies of the sample and reference intensities. Due to this, the on-axis holographic approach requires acquisition of three or four phase-shifted holograms of the same sample instance in order to isolate the sample complex wave from the unwanted waves. If these holograms are acquired sequentially, at different times, fast dynamic processes may not be recorded. However, if these holograms are acquired together, three or four camera planes are needed (or extended sensor sizes with slower frame rates are required [14]), causing registration problems between the different camera planes. On the other hand, the complex wavefront acquired by on-axis holography contains more spatial frequency data, allowing a complex wavefront with a correspondingly larger field of view (FOV), making on-axis holography suitable for imaging large static samples. Rapid on-axis holography is possible for sparse samples, such as for particle detection [15,16]. Alternatively, iterative correction processes or preliminary learning can be used [17–19]. As a solution, parallel phase-shifting digital holography is based on spatial divisions of the camera pixels, using polarization or two-dimensional (2-D) diffraction grating effects [20–23].

Alternatively, off-axis holography [1,3–11] allows a single-exposure acquisition mode with a regular digital camera by introducing a small angle between the sample and reference beams as they illuminate the camera plane, producing an off-axis hologram containing parallel linear interference fringes [24]. This enables the extraction of the complex wavefront of the sample from a single camera exposure, making off-axis holography highly relevant for acquiring the complex wavefront of dynamic samples. This single-exposure method is possible, since the parallel linear fringes

act as a carrier wave for the sample complex wavefront, and thus, in the spatial frequency domain, the CC terms, each of which contains the complex wavefront of the sample, are carried away from the origin where the DC terms, containing the sample and reference beam intensities, are located, thus creating a full separation between CC term and DC term spatial frequencies. The spatial frequency separation typically occurs across a single axis, which allows the compressing of more information along the other axes as well. This can be achieved by optical multiplexing of several holograms with different interference fringe orientations into a single multiplexed hologram, a method known as spatial holographic multiplexing. As long as CC terms and DC terms do not overlap, as shown in Fig. 1(a), full reconstruction of each of the complex wavefronts encoded is possible from a single camera exposure. Each of the multiplexed holograms can contain additional data on the imaged sample, meaning that holographic multiplexing allows for recoding of more information with the same number of camera pixels. This is beneficial for highly dynamic samples as more dynamic data can be recorded at once.

The general experimental principle in optical off-axis holographic multiplexing is the projection of two or more off-axis holograms onto the digital camera at once, so that the camera can acquire the multiplexed off-axis hologram in a single shot. Each of the projected off-axis holograms encodes a different wavefront and has interference fringes in a different orientation such that the various CC terms from all of the off-axis holograms will not overlap in the spatial frequency domain. If the experimental system is designed correctly, the multiple wavefronts encoded may be fully reconstructed without loss of resolution or FOV. A standard (nonmultiplexed) off-axis hologram contains one sample beam and one reference beam, where the beams have a small off-axis angle between them, as depicted in Fig. 1(a). This hologram can be mathematically defined as follows:

Figure 1



Comparison of standard (single) off-axis hologram of (a) two beams, sample beam S1 and reference beam R, to (b) multiplexed off-axis hologram of three beams, sample beam S1, another sample beam S2, and common reference beam R. The first column illustrates beam angles at the camera plane. The second column illustrates the resulting hologram, containing images “A” for the single hologram or both “A” and “B” for the multiplexed hologram. The third column presents the spatial frequency domains of the hologram (obtained after a digital 2-D Fourier transform of the acquired hologram). DC, autocorrelation terms; CC1, CC1*, complex conjugate CC terms from S1 and R; CC2, CC2*, complex conjugate CC terms from S2 and R; CC_x, CC_x*, cross terms from interference between S1 and S2.

$$|E_{S1} + E_R|^2 = |E_{S1}|^2 + |E_R|^2 + E_{S1}E_R^* + E_RE_{S1}^*, \quad (1)$$

where E_{S1} is the sample wave contained in beam S1 and E_R is the reference wave contained in beam R that has not interacted with the sample or has the sample modulation removed. In the spatial frequency domain (i.e., after a digital 2-D Fourier transform of the acquired off-axis hologram), as shown in Fig. 1(a), the DC terms are derived from the first two terms of Eq. (1), the sample and reference intensities, while CC1 and CC1*, each containing the sample wavefront, are derived from the last two terms of this equation, respectively. Due to the off-axis angle between the beams chosen in Fig. 1(a), being along the vertical direction, the interference fringes obtained are horizontal, and the CC terms are located along the vertical axis in the spatial frequency domain. As the CC terms are completely separate from each other and the DC terms, the complex wavefront can be reconstructed by taking a digital inverse 2-D Fourier transform of either CC term. Next, if the quantitative phase profile is needed, one needs to take the argument of the exponent of the wavefront and use a phase unwrapping algorithm to solve 2π ambiguities when needed [25].

Figure 1(b) shows the principle of optical multiplexing when two sample beams, S1 and S2, are multiplexed, using a single reference beam R , interfering onto the camera at once at a small off-axis angle. Each pair of beams encodes a different wavefront. The sample beams have interacted with the sample, while the reference beam is a beam from the same light source, but has not interacted with the sample, or has the sample modulation removed.

The multiplexed hologram depicted is given by the following equation:

$$\begin{aligned} |E_{S1} + E_{S2} + E_R|^2 = & |E_{S1}|^2 + |E_{S2}|^2 + |E_R|^2 + E_{S1}E_R^* + E_RE_{S1}^* + E_{S2}E_R^* \\ & + E_RE_{S2}^* + E_{S1}E_{S2}^* + E_{S2}E_{S1}^*, \end{aligned} \quad (2)$$

where E_{S2} is the sample wave contained in beam S2. In the spatial frequency domain (i.e., after a digital 2-D Fourier transform of the acquired off-axis hologram) shown in Fig. 1(b), the DC terms are derived from the three first terms of Eq. (2), which are the intensities of the samples and the reference. CC1 and CC1*, each containing the sample 1 wavefront, are derived from the next two terms of this equation, respectively. CC2 and CC2*, each containing the sample 2 wavefront, are derived from the next two terms of this equation, respectively. Due to the two off-axis angles between the beams chosen in Fig. 1(b), being along the vertical direction for sample 1 and the horizontal direction for sample 2, the interference fringes obtained are horizontal for sample 1 and vertical for sample 2, and they are both obtained simultaneously on the camera. In the spatial frequency domain, the CC terms originated from sample 1 (CC1, CC1*) are located along the vertical axis, and the CC terms originated from sample 2 (CC2, CC2*) are located along the horizontal axis. The last two terms in Eq. (2) are unwanted cross terms created between the two sample beams. In this case, they create a diagonal interference in the multiplexed hologram and result in an additional and unwanted CC pair (CC $_x$, CC $_x$ *) located on the diagonal axis in the spatial frequency domain. Since this multiplexed hologram contains two channels with orthogonal fringes, it is possible to reconstruct the complex wavefronts of both S1 and S2 as their corresponding CC terms do not overlap with any other term. We next crop one of the CC terms from each desired pair, say CC1 and CC2, apply a digital 2-D inverse Fourier transform, and obtain the two complex wavefronts encoded into the multiplexed off-axis hologram.

Note that there are other possible geometries for multiplexing two sample beams, such as having the two sample beams, S1 and S2, parallel to the optical axis, and using two

off-axis reference beams, R1 and R2, coming from orthogonal directions. In this case, in addition to the wanted orthogonal interferences and CC terms, we will have additional unwanted cross terms due to the interferences between S1 and R2 and between R2 and S1, which can still be set not to overlap with the wanted CC terms.

The idea of multiplexing two channels can be further extended to six channels without an overlap in the spatial frequency domain. However, in this case, one will need to avoid unwanted cross terms between nonmatching sample and reference beams, which occupy space in the spatial frequency domain that is needed for the additional wavelength channels. Generally, there are three solutions to this problem. The first one is using different polarization states [26]. The second one is by controlling the coherence properties of the illuminations either by using different lasers or wavelengths for each sample and reference beam pair [27] or by coherence gating [28,29]. In any of these solutions, nonmatching beam pairs will not interfere with each other, so that the unwanted cross terms will not be created and additional wavefronts can be compressed into the multiplexed hologram, and can still be reconstructed due to lack of overlap in the spatial frequency domain. These solutions will be reviewed in the next sections, when reviewing specific applications for off-axis holographic multiplexing. The third solution, which is limited to certain situations, is to make sure that the unwanted cross terms cannot be acquired by the camera since the camera pixel size is smaller than half of the interference fringe cycle.

Note that in Fig. 1, as well as in the rest of the paper, we assume that the hologram magnification and spatial resolution are optimized [24], and the sample is nonsparse and contains many spatial frequencies. In this case, as can be seen in the spatial frequency representations, the DC terms will occupy two times more spatial frequencies than the CC terms, and the shift in the CC terms from the origin of the spatial frequency domain is such that all terms are contained in the spatial frequency domain without overlap and without aliasing. A detailed spatial bandwidth analysis is given in the next section.

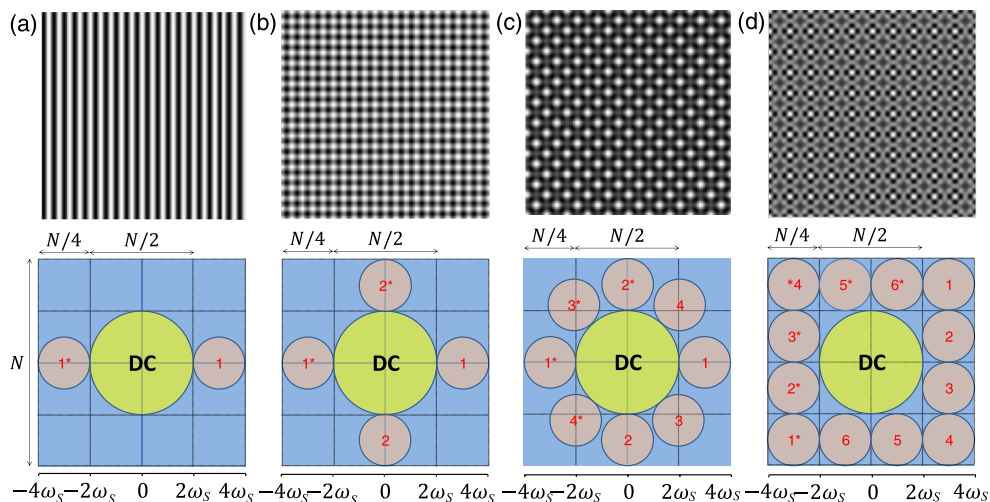
There are two types of experimental systems for off-axis holographic multiplexing: regular interferometers built around the sample and external interferometers that come after the imaging system and create the reference beam externally. In the case of regular interferometers, such as Mach–Zehnder or Michelson interferometers, one needs to integrate multiple interferometers around the sample, where each of them projects onto the camera different data on the sample and creates a different fringe orientation for the associated interference fringes. In this case, the optical system might be bulky, complicated, and hard to align. On the other hand, external modules that are located after the sample, often at the exit of the imaging system just in front of the camera, are often advantageous due to their portability as well as their common-path nature. By creating a reference beam only after the light has interacted with the sample, both reference and sample beams will travel less distance separately. Therefore, these modules have the advantage that various mechanical perturbations, such as temperature fluctuations and air flow, which are typically collected in the different interferometric arms, will have less pronounced effects on the final image and produce less temporal imaging artifacts. On the other hand, external modules assume that the sample modulation can be erased to create the reference beams externally (i.e., by spatial filtering) [10,30] or sacrifice part of the optical FOV for the reference beam, thus requiring that this part of the sample is empty [31]. Examples of these optical systems for off-axis holographic multiplexing, with focus on external modules, are reviewed within the different applications of off-axis holographic multiplexing, starting from Section 4.

2. CAMERA SPATIAL BANDWIDTH CONSIDERATIONS AND THE MULTIPLEXING LIMIT

Conventional off-axis holography uses a single sample beam and a single reference beam. In the spatial frequency domain, the off-axis hologram is transformed into two autocorrelation terms, caused by the beam intensities and located around the origin, and two complex-conjugated CC terms, located on both sides of the spatial frequency domain, each of which contains the complex wavefront of the sample. Assuming that the maximum spatial frequency of the sample beam is ω_s on both axes, as defined by the numerical aperture (NA) of the optical system used, each of the CC terms occupies a spatial bandwidth capacity of $[-\omega_s, \omega_s]$, and the autocorrelation terms occupy a spatial bandwidth capacity of $[-2\omega_s, 2\omega_s]$ [30]. This is shown in Fig. 2(a). To avoid an overlap between the CC terms and the autocorrelation terms, the center of the spatial frequency contents of the CC terms is shifted to at least $\pm 3\omega_s$, by adjusting the off-axis angle between the reference and sample beams, which requires a total spatial bandwidth of at least $8\omega_s$. In order to efficiently use the spatial bandwidth of the camera and not waste camera pixels, we need to use exactly $8\omega_s$. In other words, as shown in Fig. 2(a), if the hologram and thus its spatial frequency domain have $N \times N$ pixels, the autocorrelation terms occupy $N/2 \times N/2$ pixels, and each of the CC terms occupies $N/4 \times N/4$ pixels. In this case, the CC terms occupy only 9.8% of the spatial frequency domain.

As a partial solution, it is possible to position the CC terms on the diagonal axis, so that they can become larger, or even such that half the term is positioned over the edge of the spectrum and appears on the other side [33]. In this case, the CC terms occupy up to 24% of the spatial frequency domain. Another solution is based on hologram multiplexing. Off-axis holographic encoding typically creates an empty space in the spatial frequency domain, into which we can insert other CC terms encoding additional information on the sample. Multiplexing of off-axis holograms means obtaining an interference pattern with several off-axis interference fringe directions,

Figure 2



Schematic illustrations of off-axis holograms (top) and the coinciding spatial frequency domains (bottom) for (a) standard off-axis holography. (b) Multiplexing two off-axis holograms with orthogonal fringe directions. (c) Multiplexing four off-axis holograms. (d) 6PH, multiplexing six off-axis holograms. The numbered circles around the DC term denote the CC terms, where the coinciding complex conjugate CC terms are denoted by a number and an asterisk. Figure is modified from [32].

each of which positions a CC term in another location in the spatial frequency domain, without overlap with any other term. For example, Fig. 2(b) shows a multiplexed hologram with two orthogonal fringe directions that create two fully separable CC pairs in the spatial frequency domain. In this case, the CC terms occupy 19.6% of the spatial frequency domain. Till lately, it was accepted that one can multiplex up to four off-axis image holograms without overlap in the spatial frequency domain, as shown in Fig. 2(c) [26]. In this case, the CC terms occupy 39% of the spatial frequency domain.

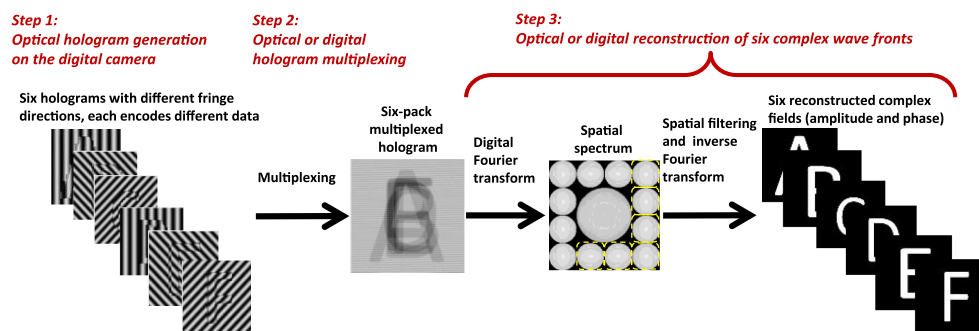
Rubin *et al.* [32] have shown two options for multiplexing six off-axis holograms without overlap in the spatial frequency domain. This principle is termed as six-pack holography (6PH). Figure 2(d) presents the multiplexed hologram and the spatial spectrum for 6PH. As shown, it is possible to position six CC terms in the spatial frequency domain without overlapping with each other and without overlapping with the autocorrelation terms. In this configuration, the total spatial frequency bandwidth capacity is $[-4\omega_s, 4\omega_s]$, and each CC term occupies a spatial frequency bandwidth capacity of $[-\omega_s, \omega_s]$.

Figure 3 presents a scheme of the entire multiplexing process. In Step 1, off-axis holograms are acquired on the digital camera. In Step 2, six holograms are multiplexed. If optical multiplexing is performed, six sample and reference beam angular combinations are projected onto the digital camera at once, so that each combination creates straight off-axis interference fringes in a different direction, and each fringe direction yields a different CC pair in the spatial frequency domain that does not overlap with any of the other five CC pairs. Alternatively, one way to perform digital hologram multiplexing is to acquire six regular off-axis holograms (e.g., while acquiring a sequence of off-axis holograms during a fast dynamic process), rotate them, and sum them to yield the multiplexed hologram.

In both cases, the multiplexed hologram encodes six complex wavefronts, but it contains real numbers only (representing the intensity of an interference pattern) and no complex numbers, and it can be sent or stored in its compressed form when needed. 6PH allows the CC terms to occupy 59% of the spatial frequency domain, which is a greater than 50% improvement compared to four hologram multiplexing. 6PH presents the optimized camera spatial bandwidth consumption for off-axis holography for *optical* off-axis hologram multiplexing, where the autocorrelation terms are simultaneously acquired.

Note that in the cases of sparse samples or nonoptimal magnification-resolution ratios, which create more empty space in the spatial frequency domain, more than six channels can be multiplexed using the same principles.

Figure 3



Schematic illustration of the 6PH multiplexing concept. Figure is modified from [32].

The analysis above considers the percentage of the area occupied in the spatial frequency domain. A more accurate analysis is given in Ref. [34]. In short, according to the Nyquist–Shannon sampling theorem, the cutoff frequency of the spatial frequency domain is half the sampling frequency. Hence, if the detector resolution is Δx , then the coinciding cutoff angular frequency is given by

$$\omega_c = \frac{\pi}{\Delta x}. \quad (3)$$

The sample maximal spatial angular frequency defined by the optical setup is given by

$$\omega_s = \frac{2\pi}{Md}, \quad (4)$$

where M is the optical magnification and d is the diffraction-limited spot diameter.

Assuming that the sample maximal spatial angular frequency defined by the optical setup is ω_s , then each of the CC terms occupies a bandwidth of $2\omega_s$, and the autocorrelation terms occupy a double spatial bandwidth of $4\omega_s$.

In on-axis holography, both the autocorrelation terms and the CC terms are centered on the zero frequency. Thus, in order to capture the full frequency range of the CC terms, a cutoff frequency of only $\omega_c = \omega_s$ is needed on both axes. This is illustrated in Fig. 4(a). In off-axis holography with multiplexing, Tahara *et al.* [33] proposed the space-bandwidth capacity enhanced (SPACE) architecture for the efficient recording of a single hologram, where each of the CC terms is split on the two sides of the spatial frequency domain, using the cyclic property of the discrete Fourier transform (DFT). This method is illustrated in Fig. 4(b). It uses a cutoff frequency of only $\omega_c = 2.5616\omega_s$ by choosing the CC shifts as $u_0 = 0.6096\omega_c$ and $v_0 = \omega_c$. Another option is illustrated in Fig. 4(c). By choosing $u_0 = v_0 = 0.6796\omega_c$, the CC terms are placed on the diagonal, enabling the compression of up to two holograms with the use of a slightly higher cutoff frequency of $\omega_c = 3.1213\omega_s$ [33]. For comparison, the 6PH architecture is illustrated in Fig. 4(d), in which six off-axis holograms with six different fringe orientations are multiplexed on the same camera plane. This architecture uses a cutoff frequency of $\omega_c = 4\omega_s$, as illustrated in Fig. 4(d). Similar configurations allowing diagonal positioning of the CC terms are presented in Refs. [35,36].

Dardikman *et al.* later suggested multiplexing eight holograms (8PH) [37] by utilizing the space occupied by the DC terms. This architecture is illustrated in Fig. 4(e). The 8PH architecture can be applied optically in the general case by removing the DC terms, as can be done by acquiring two phase-shifted holograms.

The efficiency score can be defined as follows:

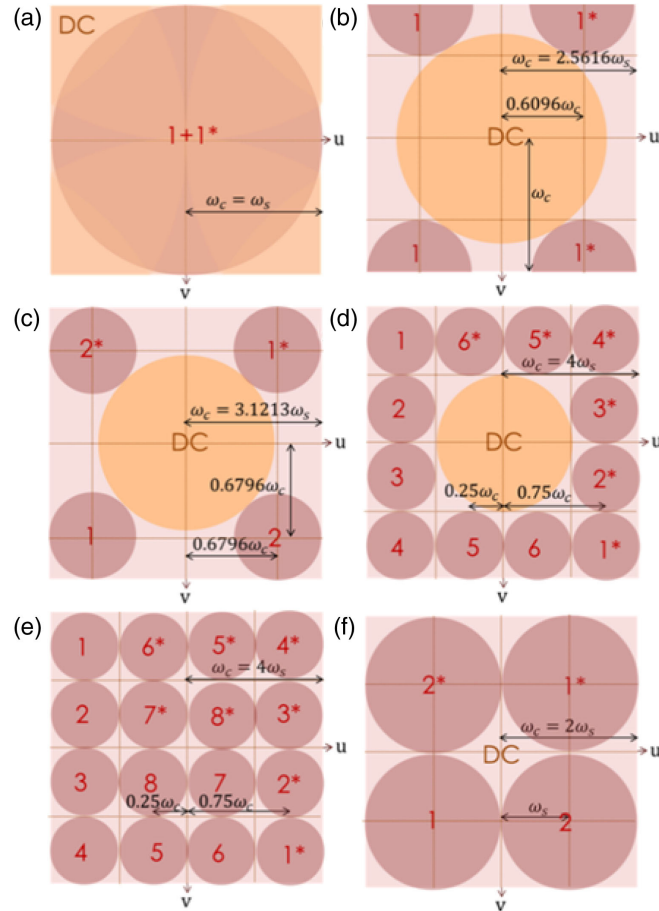
$$E_f = \omega_s / \omega_c \times N_w / N_a, \quad (5)$$

where ω_c is the cutoff angular frequency required for the method, ω_s is the maximal angular frequency of the sample, N_w is the number of wavefronts encoded in the method, and N_a is the number of acquisitions needed for reconstruction. This score expresses the ratio between the effective number of wavefronts per acquisition (N_w / N_a) and the relative cutoff angular frequency required for capturing the full frequency range of all samples without overlap (ω_c / ω_s). The calculation of the efficiency score for each of the architectures is given in Table 1.

To extend the spatial bandwidth consumption, iterative or nonlinear filtering methods can be used (i.e., Refs. [38–42] and others). These methods typically have to take

some assumptions for the sample, including weak phase or its gradient, uniform intensity, a complex amplitude confined within a quadrant in the spatial frequency domain, or requiring the analyticity condition of the Kramers–Kronig relations.

Figure 4



Schematic illustrations of the power spectra for various spatial bandwidth-efficient holographic imaging architectures, including bandwidth calculations, assuming the same number of camera pixels. (a) Optimal on-axis holography. (b) SPACE. (c) Diagonal off-axis multiplexing. (d) 6PH. (e) 8PH with the DC terms removed. (f) Diagonal slightly off-axis multiplexing with the DC terms removed. DC denotes the autocorrelation terms, and the numbered circles around it denote the CC terms, where coinciding complex conjugate CC terms are denoted by the same number with and without an asterisk. Figure is modified from [34].

Table 1. Comparison of Various Digital Holography Architectures^{a, b}

	ω_c/ω_s	N_w	N_r	E_f
Optimal on-axis	1	1	3	0.33
SPACE	2.56	1	1	0.39
Diagonal off-axis	3.12	2	1	0.64
6PH	4	6	1	1.5
8PH	4	8	2	1
Diagonal SOA	2	2	2	0.5

^a ω_c is the cutoff angular frequency required, ω_s is the maximal angular frequency of the sample, N_w is the number of wavefronts encoded, N_r is the number of acquisitions required for reconstruction, and E_f is the efficiency score.

^bTable is modified from [34].

Alternatively, slightly off-axis (SOA) holography is an experimental combination of on-axis and off-axis holography [43–47]. In this method, the off-axis concept for shifting the CC terms in the spatial frequency domain by tilting one of the beams is still used. However, here the tilting is smaller, such that the CC terms overlap with the DC term, but not with each other. Thus, the spatial bandwidth requirements are lower than those of off-axis holography, and only two phase-shifted holograms (rather than three, as in on-axis holography) are needed for reconstruction. This can be achieved because the sign of the CC terms in the second hologram, which is π shifted, is opposite to their sign on the first, such that the overlapping DC term can be discarded by simple subtraction of the two holograms. Once the DC term is eliminated, one can easily isolate one of the nonoverlapping CC terms from the spatial frequency domain. Similarly to off-axis holography, SOA holography leaves free space in the spatial frequency domain that can be used for either optical or digital multiplexing. Min *et al.* [48], for example, optically multiplexed two SOA holograms of the same scene with different wavelengths for the purpose of calculating a new hologram with a synthetic wavelength, preventing the phase ambiguity problem; Zhong *et al.* [49] presented several digital multiplexing architectures for speeding up reconstruction in SOA holography. SOA holography bandwidth considerations are presented in Fig. 4(f) and in the last row of Table 1.

Note that all multiplexed holographic channels share the same gray-scale dynamic range of the camera. Dardikman *et al.* [34] performed comprehensive numerical simulations imitating many multiplexing architectures in the presence of shot noise and compared the quality of the results both in terms of mean squared error (MSE) and SNR. It was assumed that the sample is mostly transparent and has negligible absorbance (such as individual biological cells *in vitro*). It was found that for an 8-bit detector (256 gray-scale levels), there was quality decrease, making single channel holography more advantageous. Nevertheless, when using a 16-bit detector and considering additional error factors, this issue becomes negligible, and all architectures present similar reconstruction quality. In this investigation, we did not consider the decrease of the visibility due to the fill factor of the camera pixels. Other investigations demonstrating the effect of the bit depth per hologram were conducted in Refs. [50,51].

Various applications are possible for off-axis holographic multiplexing, with focus on rapid wavefront acquisition and reconstruction. Each of them requires a different optical multiplexing system, but they all share the same principles explained in the two sections above. These applications are reviewed in the next sections.

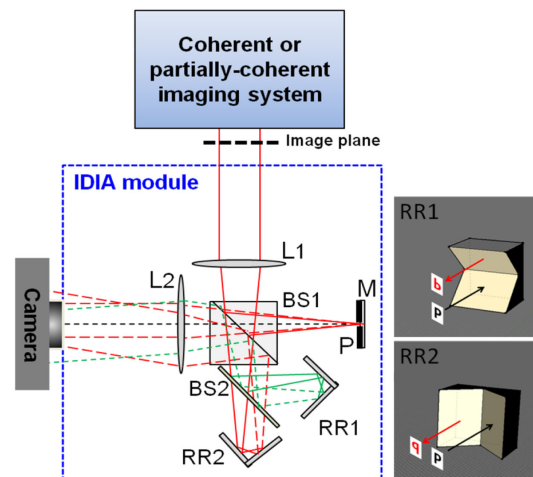
3. FIELD OF VIEW MULTIPLEXING

In Ref. [30], Girshovitz *et al.* have proposed an external holographic module that projects onto the camera two interference patterns of different fringe orientations, each of which captures the complex wavefront of a different area or FOV of the sample. This technique is called interferometry with double imaging area (IDIA). Since the two FOVs are not overlapping in the spatial frequency domain, they can be both fully reconstructed and stitched together without loss of resolution or magnification. This external holographic module is shown in Fig. 5. In this setup, instead of building two conventional interferometers around the sample (which is bulky and complicated), the magnified image from the coherently or partially coherently illuminated sample is projected onto the input of the external interferometric module instead of directly onto the digital camera. In the module, the image is optically Fourier transformed by lens L1, while being split into two beams using beam splitter BS1. One of the beams is filtered by pinhole P and reflected by mirror M, where the pinhole transfers only a

very small bandwidth around the zero spatial frequency, and thus creates a reference beam by effectively erasing the sample spatial modulation. Then, the reference beam is optically Fourier transformed back to the camera plane by lens L2, where lenses L1 and L2 are positioned in a $4f$ lens configuration. The second beam that propagates from BS1 is split again by beam splitter BS2, and both sample beams are reflected by two retro-reflectors, RR1 and RR2, and optically Fourier transformed back to the camera plane by lens L2. Each of the retro-reflectors is used to shift the center of the actual Fourier (spatial frequency) plane. The two retro-reflectors are positioned perpendicular to each other, so that one creates a Fourier-plane shift in the x direction and the other one creates a Fourier-plane shift in the y direction. This arrangement creates multiplexing of two linear, perpendicular off-axis interference fringe patterns that can be recorded simultaneously by a single camera exposure. Because the retro-reflectors also rotate the image of the sample, two mirrored images on the camera are obtained. According to this arrangement, there is an area where the two overlapping images from the two retro-reflectors are continuous. In this area, two different complex wavefronts originating from the two continuous FOVs of the sample can be reconstructed. Since these wavefronts are mirrored, one of them needs to be digitally rotated and stitched to the first one to create an image with a doubled FOV. Because the camera FOV and its acquisition frame rate are interchangeable, the IDIA technique encapsulates the capability of increasing the camera frame rate without decreasing the original reconstructed FOV, since instead of doubling the camera FOV, the acquisition frame rate can be increased, while using half of the camera pixels. Figures 6 and 7 show several experimental results of quantitative phase imaging of stationary (Fig. 6) and dynamic (Fig. 7) samples acquired with the external multiplexing module presented above. Further extensions of the IDIA principles to broadband holography and to flipping interferometry [31] have been presented in Refs. [52,53], respectively.

Reference [26] extended this FOV holographic multiplexing approach to multiplexing three complex wavefronts of three FOVs of the sample into a single multiplexed hologram. In this case, the problem of unwanted cross terms became more critical,

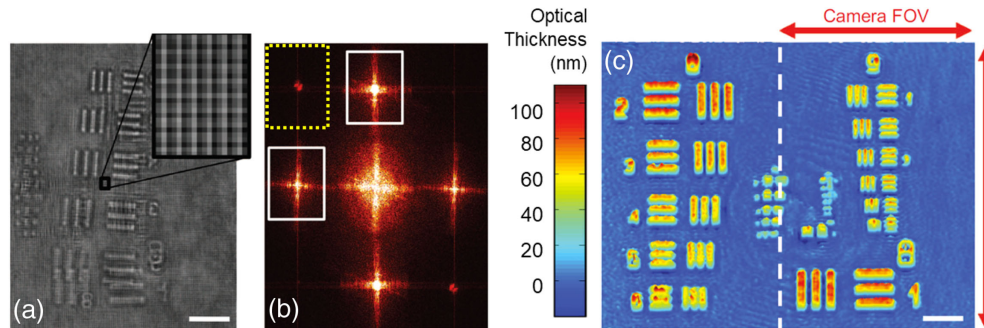
Figure 5



IDIA module for optical multiplexing of two off-axis holograms. The module is connected to the digital camera port at the output of a coherent or partially coherent imaging system. The retro-reflectors are orthogonal to each other. Right inset, 3-D diagram of the retro-reflectors and their effect on the incoming image. BS, beam splitter; L1 and L2, lenses in a $4f$ configuration; M, mirror; P, pinhole; RR1 and RR2, retro-reflectors. Figure is modified from [30].

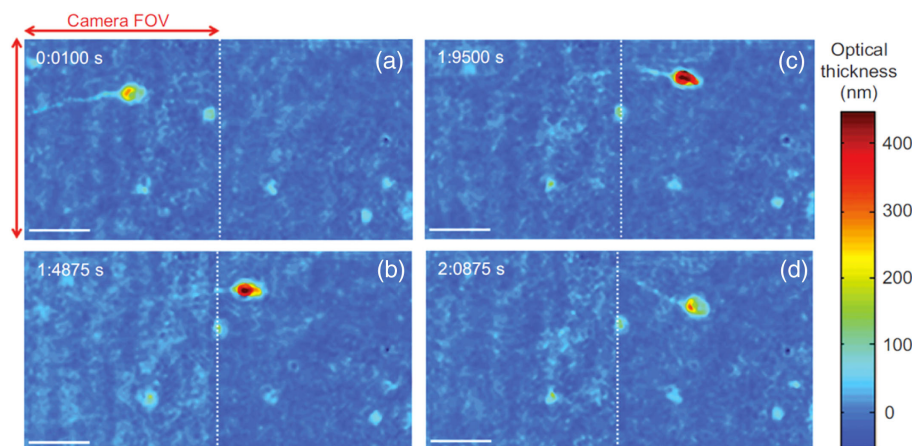
so polarization coding was used to avoid at least one of the unwanted cross terms. The external module for FOV tripling is shown in Fig. 8(a). An inverted transmission microscope is illuminated by a He-Ne laser, containing a microscope objective and a tube lens [not shown in Fig. 8(a)]. The image of the sample is created at the output of the microscope, where the three-FOV-multiplexing module is located. The image at the microscope output is Fourier transformed by lens L1 and split by beam splitter BS1 to the reference and sample paths. Spatial filtering is used in the reference path to erase the sample modulation by using pinhole PH located in front of a mirror. In the sample path, the beam is split into three sample beams by beam splitters PBS and BS2. At the exit of each beam splitter, retro-reflectors reflect the beams back in

Figure 6



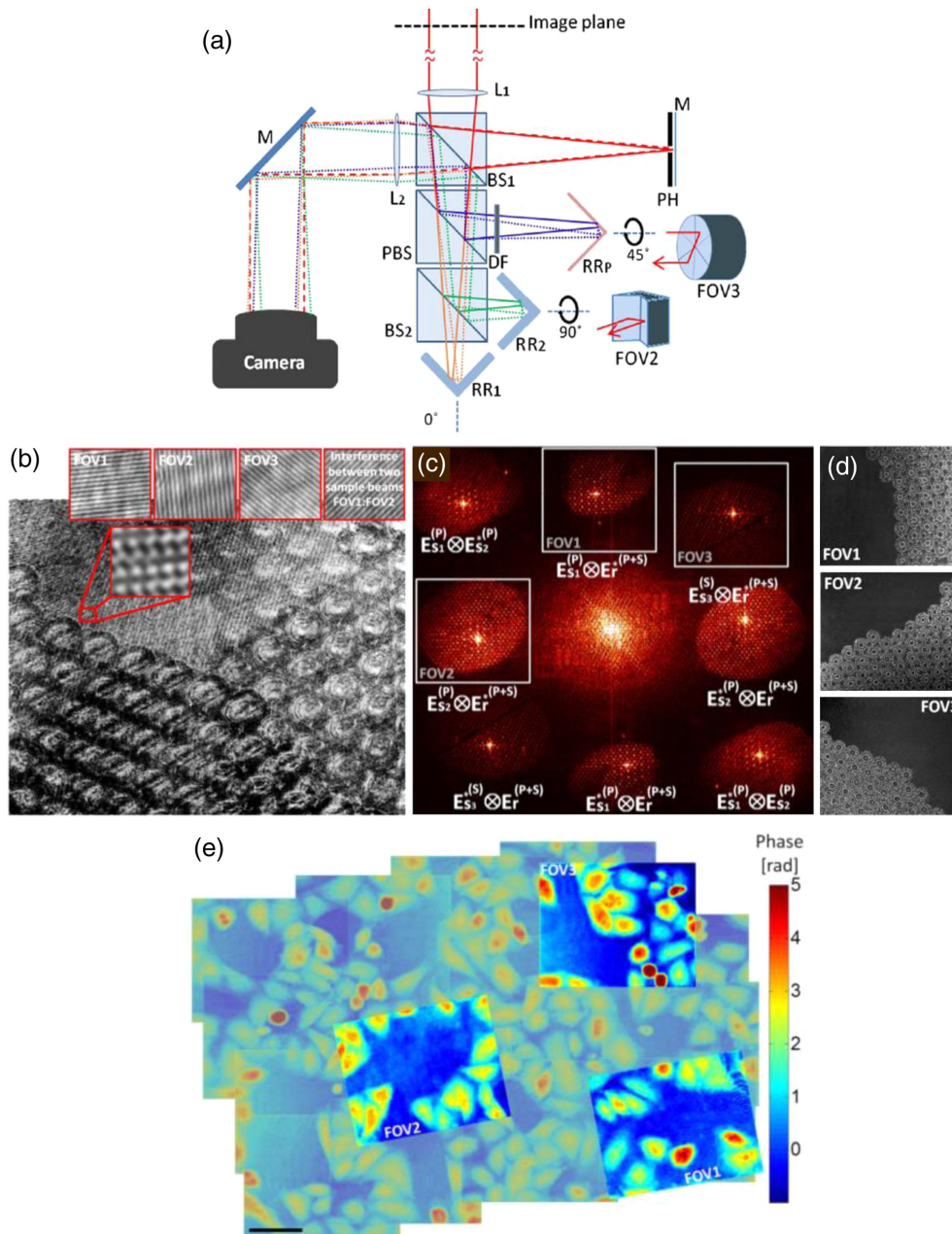
Optical multiplexing of two off-axis holograms of an optically transparent 1951-USAF test target under low-coherence illumination. (a) Multiplexed off-axis hologram recorded in a single digital camera exposure using the IDIA module. (b) Spatial Fourier transform of the multiplexed hologram. The white boxes mark the desired CC terms, and each is generated from another reference-sample beam pair and encodes a different FOV of the sample. The yellow dashed line box marks the unwanted cross term between the two sample beams. (c) Final optical thickness map of the test target, obtained by stitching together the two thickness maps. The white scale bars represent $10\ \mu\text{m}$. Figure is modified from [30].

Figure 7



Quantitative optical thickness maps with doubled FOV of a swimming human spermatozoon, as recorded by the IDIA technique, enabling the acquisition of the fast dynamics of the spermatozoon with fine details on a doubled FOV. The white dashed line indicates the location of the stitching between the two FOVs. The white scale bars represent $10\ \mu\text{m}$. A video, demonstrating the ability to record fast dynamics, is shown in [30].

Figure 8



(a) Optical system for multiplexing three FOVs using three rotated retro-reflectors and orthogonal polarization states to avoid one of the two unwanted cross terms [26]. This module is positioned at the output of a transmission microscope. L1, L2, lenses; POL, 45° polarizer; BS1, BS2, beam splitters; PBS, polarizing beam splitter; DF, density filter; M, mirror; PH, pinhole; RR1, RR2, retro-reflectors made out of two mirrors connected at a right angle; RRP, retro-reflector made out of a total internal reflection prism. (b) Multiplexed holograms containing three FOVs of microbeads. (c) The coinciding spatial power spectrum. (d) The three wrapped phase profiles reconstructed from the multiplexed hologram. (e) Resulting quantitative phase imaging of HeLa cell culture with tripled FOV. In muted colors, the scanned FOV (which is larger than the camera regular FOV). In vivid colors, the three quantitative unwrapped phase images reconstructed from a single multiplexed hologram, acquired simultaneously without any scanning. Figure is modified from [26].

a different angle. Retro-reflectors RR_1 and RR_2 are rotated at 90° compared to each other, while the beam reflected from retro-reflector RR_p is rotated at 45° compared to the beams from RR_1 and RR_2 . Each of the three sample beams is then combined with the final reference beam using the beam splitters, and inverse Fourier transformed onto the camera by lens L_2 . Three off-axis interferences are created on the camera, with fringes rotated at 45° compared to each other. Each retro-reflector also rotates the sample image. Since the projected sample image is larger than the camera sensor size, three sample FOVs are projected onto the same camera sensor at once. Since the sample is initially illuminated by a 45° -polarized light by using a linear polarizer POL in front of the laser, the reference beam has both P and S polarization states. After splitting the beam in the polarizing beam splitter PBS, S polarization is reflected, and P polarization is transmitted. Therefore, the two FOVs reflected by RR_1 and RR_2 are P -polarized, and after they interfere with the P -polarized part of the reference beam, two orthogonal off-axis holograms are created on the camera. RR_1 and RR_2 are built by two mirrors connected at 90° . RR_p is a total internal reflection prism, turning linearly polarized light into elliptically polarized light, so that the S polarization is not blocked by the PBS. The multiplexed hologram of microbeads is shown in Fig. 8(b), and the coinciding spatial spectra are shown in Fig. 8(c), with the associated polarization states marked by superscripts. As can be seen, using orthogonal polarization states, the cross terms from two of the sample beams are avoided. This allows us to use more empty space in the spatial frequency domain for the third sample, so that all three FOVs of the microbeads can be reconstructed, as shown in Fig. 8(d). However, since only two orthogonal polarization states are available, there are still unwanted cross terms, and the spatial frequency domain is fully occupied. This implies that in order to add more sample beams, without overlap in the spatial frequency domain, other effects such as different wavelengths or coherence gating should be used.

Several additional experimental demonstrations were provided in this paper; for example, Fig. 8(e) shows quantitative phase imaging of live HeLa (human cervical cancer) cell culture. As presented in Fig. 8, a broad area of 4×4 frames was first scanned using a single FOV holography (presented as the muted-color background). Then, the module presented in Fig. 8(a) was used for recording three FOVs from the sample simultaneously [as presented in Fig. 8(e) in vivid colors], while enabling quantitative imaging of a larger cell population.

Finally, it should be noted that FOV multiplexing can also be viewed in the opposite direction. That is, instead of retrieving an enlarged synthetic FOV from the multiplexed hologram, it is possible to penalize the optical FOV to get improvement in other domains. Thus, a lot of effort has been expended during the last few years to reduce the useful FOV in order to retrieve complex amplitude information of the sample using off-axis holographic configuration [19,30–38]. The common key point to all those approaches is to save a clear area in the FOV for reference beam transmission in order to allow holographic recording by different means at the detection plane. As a consequence, the available FOV for sample analysis is reduced, but quantitative phase information is retrieved in a single shot. Most of those approaches have an additional added value: they are mainly applied in conventional bright-field microscopes without coherent testing capabilities. So the result is a microscope, which is converted into a holographic one using common-path interferometric layouts.

Following this line, Lloyd's mirror has been used as interferometric architecture to allow off-axis holographic recording [54]. The authors validated the novel concept by imaging red blood cells using a $45\times$, 0.65 NA microscope objective and studying their membrane vibrations in time. Micó *et al.* [55] reported on a technique where the input plane is spatially multiplexed to allow reference beam transmission in a

common light-path with the imaging branch. The sample is placed in a side-by-side configuration with the reference area, and the overlapping between both areas (holographic recording) is provided by using a diffraction grating at the image space. The proposed method was experimentally validated in a regular Olympus BX-60 upright microscope for different types of biological samples. The lateral shearing interferometric (LSI) approach was first introduced by Singh *et al.* [56] and lately expanded and generalized under different conditions by Seo *et al.* [57], as well as Kim and Kim [58]. In LSI approaches, holograms are obtained by two laterally sheared object beams, and they include not only DC bias and twin images but also the undesired duplicate images, which result from the two sheared object beams involved in interference. The DC term and twin image can be removed by conventional spatial Fourier filtering using an off-axis configuration, which in LSI is achieved by using a wedge optical window or a pellicle beam splitter and optical mirror for the shearing [58]. The duplicate image problem is avoided by considering a thick optical window, thick enough to allow image separation [57]. Similar to Ref. [55], Han *et al.* [59] proposed a spatial division of the input FOV into the regions (sample and two reference areas) to allow orthogonally polarized reference beam transmission in order to record an angular multiplexing polarization hologram for measuring the Jones matrix parameters of polarization-sensitive or birefringent materials in a single shot [59]. Additional implementations for quantitative phase imaging were proposed by Sun *et al.* [60] and Ebrahimi *et al.* [61], where off-axis interferometric recording was obtained by using both a Fresnel bimirror and biprism, respectively. Following the original idea from Leith and Upatnieks in the 1960s, Sun *et al.* [62] reported on a beam splitter cube interferometric layout where the reference beam was redirected toward the recording plane by using a wedged glass plate.

FOV multiplexing can also be employed in a common-path multibeam interferometry with small shearing [63–65], producing off-axis multiplexed holograms with compressed information on spatial derivatives of the sample phase distribution. A simple crossed binary amplitude Ronchi grating [66], amplitude checker grating [67], or an advanced quadri-wave diffraction structure composed of an appropriately frequency-matched crossed binary amplitude grating and a phase checker grating [68] are frequently applied. The hybrid amplitude cross-checker [69] and randomly encoded [70] gratings recently emerged as diffraction-efficient approaches. The diffraction grating profile determines the multibeam interference angles, hence enabling the tailoring of the Fourier spectrum of the off-axis multiplexed hologram. After applying Fourier-transform-based calculation on at least two orthogonal spatial derivatives, the underlying phase function of interest can be computed utilizing an integration engine [71,72]. Shearing single-shot multibeam off-axis-multiplexed holography has many applications. For example, quadri-wave lateral shearing interferometry was employed for wavefront sensing [73], quantitative phase imaging [74], and quantitative retardance imaging [75], whereas 3×3 -beam [76] and five-beam [77] interferometry were employed for extended wavefront gradient sensing.

4. DEPTH-OF-FIELD MULTIPLEXING AND DISPLACEMENT AND SHAPE MEASUREMENTS

Digital holography provides unique access to 3-D object information through sequential numerical propagation of reconstructed complex amplitude to different focal planes, e.g., enabling 3-D live cell tracking in an imaged volume [78]. Nonetheless, the potential attractiveness of simultaneously multiplexing information coming from different layers is compelling. This idea can be traced back to the so-called multiplane imaging, commonly used in microscopy, particle tracking, and medical imaging, where diffraction gratings (binary amplitude [79] and phase [80]), beam splitters

[81], or spatial light modulators (SLMs) [82] are employed for sharp multiplexing of several focal planes in a single camera acquisition. Single-shot digital holographic approaches, reviewed in this subsection, use coherent recording and numerical reconstruction to achieve depth-of-field multiplexing.

Reference [83] has shown that by using hologram adaptive computational deformation, it is possible to control the numerical reconstruction distance and alter it spatially to provide a sharp image of a tilted object. Numerical propagation of tilted complex amplitude to ensure object sharpness in a wide FOV is a challenging task [84], and can be seen as a good example of holographic depth-of-field multiplexing. A fully automated approach [84] is executed in two parts: first the local sharpness estimation leads to rotation axis localization, and next the angular orientation is devised, maximizing the focus of optical fields reconstructed in many subsequent tilted planes.

Reference [85] demonstrated that by modifying the numerical reconstruction process of off-axis digital holograms by adding a synthetic diffraction grating effect, it is possible to image three planes at different depths simultaneously. Numerical grating offers increased flexibility over a physical grating. Moreover, the authors have shown that two different wavelength channels can be obtained in focus simultaneously by a single off-axis multiplexed hologram.

Reference [86] proposed a hologram reconstruction algorithm to image multiple planes at different depths simultaneously. A shift parameter that accounts for the coordinate system transverse displacement of the image plane at different depths was introduced in the diffraction integral kernel. Combination of the diffraction integral kernel with different shift values and reconstruction depths yields multiplane holographic imaging in a single reconstruction. A review of holographic depth-of-field multiplexing is provided in Ref. [87].

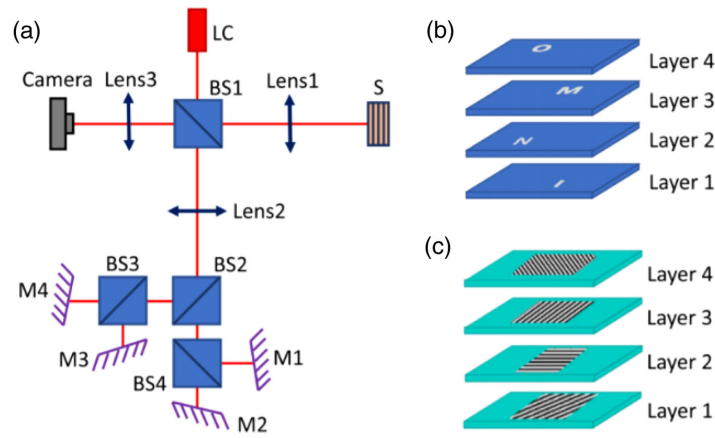
Reference [88] presented multiplexing of multiple sections in a low-coherence interferometric setup, which enables the simultaneous amplitude and phase reconstruction of multiple sections in multiplane samples in a single camera acquisition with rejection of out-of-focus debris. The method is applicable to cases in which the depth of field is large; thus, the entire 3-D sample is in focus on the camera. In these cases, one cannot know the order of layers in the 3-D sample. To solve this problem, the authors divided the depth of field into several layers, each creating a different fringe orientation on the camera simultaneously, and the different layers do not interact with each other due to coherence gating. Optical layout of the setup is presented in Fig. 9, while exemplifying results are shown in Fig. 10.

Spatial multiplexing can also be applied to perform 3-D displacement measurements, for both metrology and biomedical applications [89–92]. In addition, spatial multiplexing can be applied to perform 3-D shape measurements, followed by phase unwrapping with multiple illumination angles [93–95]. Imaging from multiple viewpoints can be used to improve the 3-D position measurements, which is typically carried out for particle tracking [96–98].

Deep learning approaches have constantly increasing impact on optical techniques, especially digital holography. By virtue of this, several groups have proposed advancements in optical depth-of-field multiplexing based on autofocusing [99–101]. Reference [99] reported on a versatile (from on-axis to off-axis) coherent recording scheme with automatically maintained focus employing machine learning. The authors posed autofocusing as a regression problem, with the focal distance being a continuous response corresponding to each hologram, converting distance estimation to hologram prediction [solved by designing a powerful convolutional neural network (CNN) trained by a set of holograms acquired *a priori*]. Reference [100]

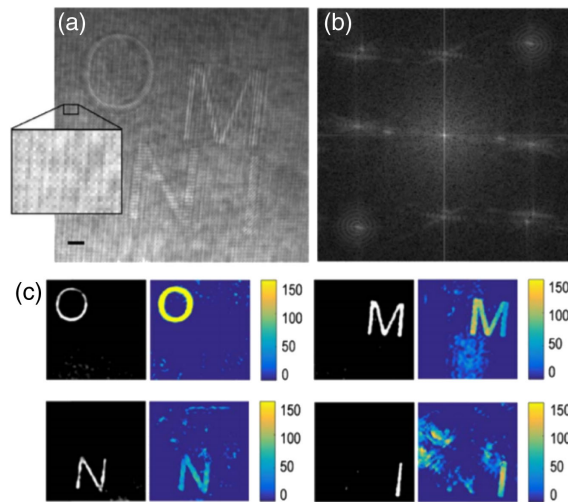
describes a CNN-based approach that extends the depth of field and increases the reconstruction speed in holographic imaging. For this, a CNN was trained by using pairs of randomly defocused backpropagated holograms and their corresponding in-focus phase-recovered images. After this training phase, the CNN takes a single

Figure 9



(a) Schematic representation of the optical setup for depth-of-field off-axis holographic multiplexing. LC, low-coherence light source; Lens1, Lens2, Lens3, lenses in $4f$ lens configurations; S , multilayer reflective sample; BS1-BS4, beam splitters; M1-M4, mirrors that provide the desired spatial frequencies in the off-axis interference fringes. (b) Multilayer sample comprising four coverslips, each imprinted with a reflective letter: O, M, N, I. (c) Unique fringe orientation captured from each layer of the sample indicating the axial location of each layer. Figure is modified from [88].

Figure 10



Depth-of-field off-axis holographic multiplexing results: optical sectioning obtained by off-axis holographic multiplexing for the four-layer sample described in Fig. 9(b). (a) Multi-mplexed off-axis hologram acquired in a single camera exposure. The scale bar represents $130\ \mu\text{m}$ on the sample. (b) Corresponding power spectra containing four distinct cross-correlational pairs. (c) Reconstructed amplitude (left) and unwrapped phase (right) profiles obtained by cropping the corresponding cross-correlational elements in (b), enabling simultaneous reconstruction of all four-layer complex wavefronts from a single camera exposure. The color bar represents the height values in nanometers. Figure is modified from [88].

backpropagated hologram of a 3-D sample as input to rapidly (noniteratively) achieve phase recovery and reconstruct an in-focus image of the sample over a significantly extended depth of field. The presented approach was positively verified using on-axis holograms; however, the off-axis regime could be approached by similar means. Reference [101] can be seen as a generalization of Ref. [100] onto both incoherent and coherent illumination. Authors used addition of one or a few off-axis illumination sources (e.g., LEDs) to allow focus correction from a single image with this illumination. Neural network architecture, the fully connected Fourier neural network, was designed exploiting an understanding of the physics of the illumination to make accurate predictions without any specialized hardware.

5. WAVELENGTH MULTIPLEXING

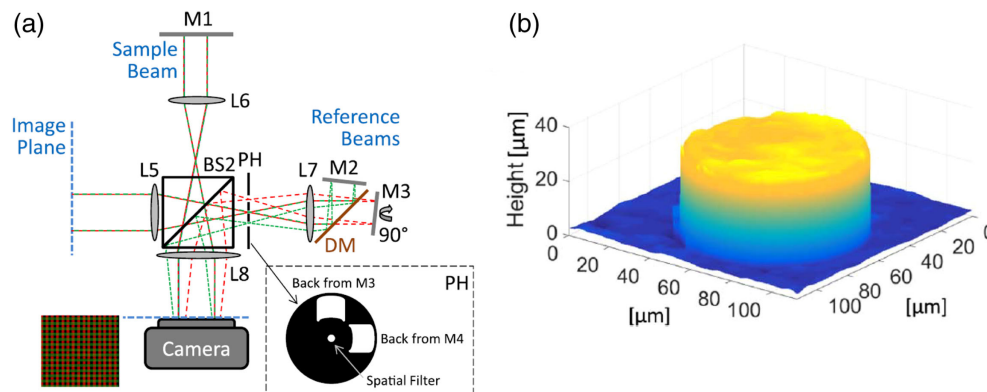
When multiplexing various illumination wavelengths, unwanted cross terms are not usually an issue as different wavelengths of light do not interfere with each other. However, this does not necessarily make wavelength multiplexing easier to implement, as one must consider that the fringe frequency and, thus, the positions of the CC terms are dependent on both the off-axis angle and the wavelength. In addition, the diffraction-limited spot size and, thus, the size of the CC terms are also dependent on the wavelength. Finally, if multiple wavelengths are being used, then chromatic aberrations become a concern. One example of a system that multiplexes multiple wavelengths is the system from Ref. [27]. In this article, the system is composed of a Twyman–Green interferometer and an assembly of beam splitters used to direct red and green light from two lasers into the system. One entrance receives a combined illumination beam of red and green light, while the second entrance receives two off-axis reference beams, one red and one green. The illumination beam is diffracted and reflected by the sample and then combines with the reference beams to produce the multiplexed hologram on the camera.

Multiplexing of several off-axis holograms acquired with different illumination wavelengths of the same sample instance (rather than different FOVs, etc.) can be used for both multiwavelength phase unwrapping and holographic spectroscopy. Regarding the first application, since the quantitative phase retrieved is 2π periodic, objects that are optically thicker than the illumination wavelength are wrapped and subject to phase measurement ambiguity. Therefore, a 2-D phase unwrapping algorithm is applied digitally to obtain continuous phase reconstruction [25]. However, these algorithms are computationally demanding, but more importantly, they might fail when a large phase discontinuity is encountered. Alternatively, an experimental solution to the phase ambiguity problem is two-wavelength holography [102], in which two holograms with different illumination wavelengths are acquired, and the wrapped phase profile is extracted from each of them separately. Then, a new phase profile can be calculated based on both phase profiles, where the new phase profile has a large synthetic wavelength, significantly increasing the unambiguous phase range [3,27,103]. Since two different holograms are needed, the acquisition should be faster than the sample dynamics. To solve this problem, Kühn *et al.* [27] used simultaneous two-wavelength holography by multiplexing two beams of different wavelengths on the same sensor, providing real-time holographic capabilities. Their system was based on two Mach–Zehnder interferometers, built around the sample, creating two separate reference beam paths, one for each wavelength, so that on the camera they obtained two off-axis holograms of the sample simultaneously, with 90° rotated fringe direction in relation to each other. Other methods for separating the two wavelengths in simultaneous dual-wavelength interferometry include using a color Bayer-mosaic camera [104] and polarization [105]. Variants of the techniques described above were

used for examination of samples with large topography changes, such as porous coal samples [106] and biological samples [107]. These methods require two separate reference beams, which are separate from the sample along most of the optical path, and thus are more prone to mechanical noise, as all three beams may not be subjected to the same vibrations.

Self-interference interferometric techniques for dual-wavelength holography have evolved over the past decade [10,108,109], allowing more stable systems with a decreased temporal phase noise due to nearly common-path interferometric geometry. In these systems, both the reference and the sample beams are formed from the image of the sample itself. The reference beam can be generated externally, after the output image plane of the optical system, from a spatially filtered version of the image, effectively erasing the sample spatial modulation from one of the beams, while the off-axis interference is realized by a retro-reflector [10] or a diffraction grating [109]. In Ref. [110], Turko *et al.* presented a dual-wavelength external holographic microscopy module for quantitative phase imaging of 3-D structures with extended thickness range. This was done by simultaneous acquisition of two off-axis holograms, each at a different wavelength, followed by generation of a synthetic wavelength, which is larger than the sample optical thickness. This allows simultaneous two-wavelength unwrapping of samples that are too thick to be imaged in regular single-wavelength holography. As shown in Fig. 11(a), in this holographic module, the beam was Fourier transformed by lens L5, while being split into sample and reference beams by beam splitter BS2. The sample beam was Fourier transformed by lens L6, reflected by mirror M1, and projected onto the monochrome camera through lenses L6 and L8, so that the images were projected onto the camera from both wavelength channels at once. In the reference beam arm of BS2, at the Fourier plane of lens L5, a spatial filter made out of pinhole PH was placed, which selected only the low-frequency spatial information and effectively turned it into a reference beam. Then, lens L7 was used to Fourier transform the beam back into the image domain, while separating the two-wavelength beam into its two wavelength channels using dichroic mirror DM.

Figure 11



(a) External holographic module for multiplexing two wavelength channels into a single multiplexed hologram [110]. L5–L8, achromatic lenses; BS2, beam splitter; PH, pinhole plate; DM, dichroic mirror. A monochrome digital camera is used to acquire the two orthogonally rotated off-axis holograms of different wavelengths at once. (b) Reconstructed height profile of a 30.5- μm -high, 70- μm -wide copper pillar, obtained by the module shown in (a) when connected at the output port of a reflection microscope. The two wavelength channels are used for simultaneous two-wavelength phase unwrapping, enabling profiling of this thick sample without 2π phase ambiguities. Figure is modified from [110].

Each of the channels was then backreflected by slightly tilted mirrors, M2 and M3, and projected to the camera at an off-axis angle through lenses L7 and L8. The relative angle between mirrors M2 and M3 was adjusted, such that each wavelength channel created an orthogonal off-axis interference fringe direction with respect to the other channel, and thus a single multiplexed off-axis hologram from the two wavelength channels can be recorded by the camera at a single exposure. The two phase profiles from the two wavelength channels were processed to create a new phase profile with no 2π phase ambiguities. Figure 11(b) shows an example of height profiling of a round copper pillar with height of $30.5\ \mu\text{m}$ and a certainty of $7\ \mu\text{m}$, as obtained by the system shown in Fig. 11(a).

The main problem of two-wavelength phase unwrapping is the inherent amplification of noise that comes with the calculation of the synthetic wavelength phase profile, which results in a decrease in the sensitivity [103]. In order to optically unwrap the phase map of thick objects, but still keep the sensitivity as that of a single wavelength, three-wavelength phase unwrapping was introduced [111–114]. Using a third-wavelength hologram, one can produce phase maps of three gradually decreasing synthetic wavelengths, and then use hierarchical optical phase unwrapping [112]. In general, when wavelength scanning is used [113,114], the sample might be subjected to vibrations, and the acquisition throughput may be slower as well, which can be problematic for acquiring dynamic samples. Turko *et al.* [115] have proposed simultaneous three-wavelength holographic multiplexing acquisition, which is able to acquire the quantitative phase profiles of thick samples with the same level of noise as that of a single wavelength acquisition.

Another application of simultaneous multiwavelength holography is holographic spectroscopy and refractive index dispersion [116–119], which is useful for various measurements of biological cells *in vitro*. A third application is using the multiple wavelength measurements to decouple refractive index and physical thickness from the phase measurement [120] (since phase is proportional to the optical thickness, which is defined as the product between refractive index and physical thickness [1]). In cases where the refractive index of the sample is dependent on the wavelength, this decoupling problem can be solved using the multiple phase profiles, simultaneously provided by the multiplexed hologram. Note that in some of these papers [117,118,120], the multiplexing is not spatial bandwidth efficient, since it is done across one diagonal axis in the spatial frequency domain.

6. MULTIPLEXING FOR SYNTHETIC APERTURE SUPER-RESOLUTION

Optical imaging systems are restricted both axially and transversally in resolution due to the wave nature of light [121]. This fact has been well-known since the 19th century, when the German physicist Ernst Abbe explained, without mathematical foundations, the relation between NA, illumination wavelength (λ), and resolving power (r) for image formation in microscopy. Some years later, Helmholtz derived the maximum resolution achievable in microscopy, which can reach up to one-half of the illumination wavelength [122], Lord Rayleigh published a manuscript with the mathematical foundation of Abbe's discovery [123], and Porter involved Fourier's theorem in the development of Abbe's theory and demonstrated the power of Fourier optics in image formation by placing different masks (diffraction gratings) in the back focal plane of a microscope lens [124].

Essentially, every optical system under collimated illumination has a bandpass truncation limiting the transversal resolution to a value of $r = k\lambda/(n \sin q)$, where k is a constant that depends on the imaging system configuration (for instance, it has a value of 0.82 for coherent imaging systems with circular apertures [125–127]), and

q is the one-half of the angular aperture of the microscope objective. Usually the NA of the imaging is $NA_{\text{imag}} = n \sin q$, and the previous equation is modified for a noncollimated beam of illumination according to $r = k\lambda / (NA_{\text{imag}} + NA_{\text{illum}})$, where NA_{illum} relates to the NA of the illumination. Thus, the maximum achievable resolution for air-immersed imaging systems is $r = k\lambda/2$, that is, approximately half the illumination wavelength, which, for example, means ~ 200 nm for blue illumination. This is a strong barrier in optical microscopy since a wide range of processes and events takes place at smaller scales. Moreover, it is quite common in microscopy to use low/medium NA microscope objectives since they possess attractive properties, such as longer working distances, larger fields of view, and reduced prices, at the expense of poorer resolving power (large r values).

Currently, coherent illumination is widely used in optical microscopy for a vast range of applications [128–130]. In order to simplify the optical configuration, coherent light is usually inserted as a collimated beam, meaning that $NA_{\text{illum}} = 0$ and the resolution limit is penalized to be $r = k\lambda / NA_{\text{imag}}$ with a minimum value of ~ 400 nm for blue illumination (even less in cases of medium/low NA lenses). To increase the NA_{imag} value without replacing the NA of the microscope objective lens itself, it is possible to replace the surrounding medium (typically air) between the object and the sample by a medium with a higher refractive index value, thus originating the concept of immersion microscopy [131]. It is also possible to increase NA_{imag} synthetically, by selecting only specific directions of illumination in order to diffract toward the objective lens different spatial frequency content of the sample within the NA_{imag} allowed. Those additional spectra are then transmitted through the regular lens aperture and used to generate a synthetic spectrum that effectively has a larger NA_{imag} , providing an image with better resolution in comparison to the regular one. This super-resolved image can be equivalent in resolution to the one provided by a lens having a larger physical NA_{imag} . This procedure is usually known as super-resolution by synthetic aperture (SA) generation [132]. Nowadays, SA generation in optical microscopy is a vividly blossoming technique with many different applications [133]. In this section, we will review super-resolution holographic techniques based on SA, which allow single-shot acquisition by acquiring a multiplexed hologram.

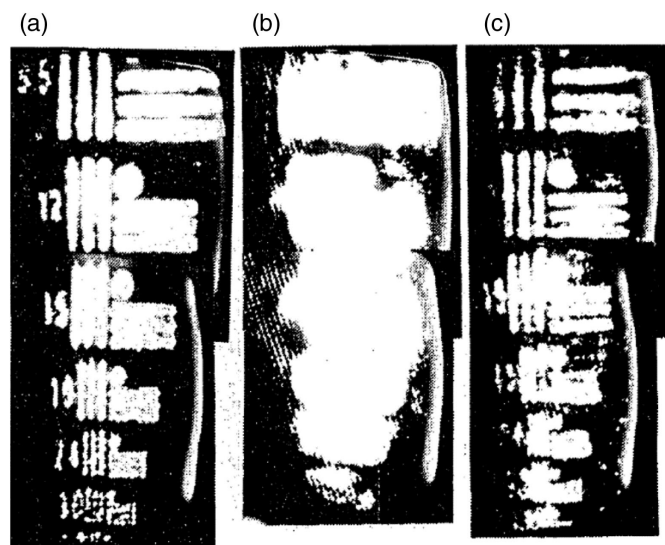
The first approach regarding super-resolution using multiplexed holography seems to date back to the early 70's [134]. In their work, Ueda and Sato presented a simple optical method for improving the spatial resolution by using time multiplexing. The authors recorded a multiexposed hologram composed by the addition of several bandpass images of the input object obtained sequentially under different oblique illuminations (usually termed as angular multiplexing by tilted beams). Off-axis holographic recording was accomplished by reinserting a set of complementary off-axis reference waves at the hologram plane, complementary to each oblique beam. Although the achieved synthetic NA was extremely low (~ 0.0038 NA), this approach was the first to achieve time multiplexed super-resolution using off-axis illumination and holographic tools. Two years later, Ueda *et al.* extended the capabilities of the former approach by including a mathematical derivation of the method and by applying the approach to 2-D objects [135]. Again, the synthetic NA values were extremely low (~ 0.0051 NA), as a consequence of the experimental configuration. But, one year later, Sato *et al.* improved the performance of their approach by considering a microscope lens ($10\times$, 0.13 NA) [136]. Digital acquisition of the different holograms using a video camera and the digital superposition of them to synthesize the super-resolved image in a posterior stage was implemented. Again, time multiplexing was applied to the recording of the different holograms multiplexed, so no single-shot capability was demonstrated. But, finally, Sato *et al.* proposed a new approach for

real-time super-resolution by means of an ultrasonic light diffractor and a TV visualization system [137]. The system had greater simplicity, and it was able to produce one-dimensional (1-D) and 2-D real-time super-resolved imaging with extremely low synthetic NA because of the low diffraction angles produced in the ultrasonic light diffractor. Nevertheless, this method can be considered as the first single-shot super-resolution approach by multiplexing holography. Figure 12 includes the experimental results for a 2-D super-resolution effect considering a resolution test target where (a) corresponds with the full resolution image obtained with 0.037 NA and without the ultrasonic waves, (b) shows the image with limited resolution after closing the iris (0.0006 NA approx.) and without the ultrasonic waves, and (c) shows the super-resolved image retrieved from the configuration in (b) but activating the ultrasonic light diffractors.

After that, many super-resolution approaches by multiplexing different degrees of freedom in holography has been reported in the literature. From a first review manuscript in 1984 [138] to more recent references [132,133,139–141], the reader can realize the vast number of applications provided by super-resolution imaging techniques, but only a few are capable of working in single-shot exposure.

The next step in single-shot super-resolution techniques was provided by Leith *et al.* around 30 years ago. In a first paper [142], they demonstrated the 1-D super-resolution effect using spatially incoherent illumination in an interferometric layout formed from diffraction gratings. Essentially, the system worked as a set of tilted beams with different propagation angles that, in one arm of the system, illuminate the input object, which is imaged by an imaging system with reduced aperture and, in the other arm, provides a set of tilted beams for the interferometric recording being coherent with its corresponding illumination beam but incoherent with the others. In the imaging branch, different spatial frequency content was transmitted through the limited aperture because of the tilted beam illumination, which interfered with its corresponding mutually coherent reference beam coming from the reference branch.

Figure 12



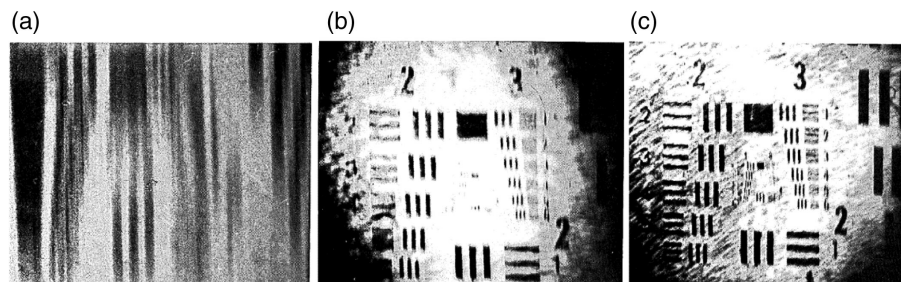
Experimental results for single-shot 2-D super-resolution by Sato *et al.* [137]. (a) Conventional image with 0.037 NA and with light diffractors off. (b) Image restricted in resolution by closing the iris until 0.0006 NA and with light diffractors off. (c) The super-resolved image coming from (b) with light diffractors on. Figure is modified from [137].

The number of tilted beams coming from the reference branch is selected by effective image size of the illumination source image—the larger the source, the larger the effective aperture and the better the resolution limit. Finally, the recorded pattern was treated as a hologram, and the reconstruction was observed in the first diffraction order. Figure 13 includes the experimental validation where a resolution test target is first imaged under the low-resolution imaging system in Fig. 13(a), and then the proposed 1-D super-resolution technique is applied for two different source sizes [Figs. 13(b) and 13(c)] controlled by the ration of the focal lengths used in the layout.

A theoretical modification of the previous layout [142] was presented by Leith a few years later [143], and later on, Sun and Leith reported on the generalization of Lukosz's approach [144,145] by considering optical diffusers in synchronized movement instead of diffraction gratings [146]. As in Lukosz's idea, the diffusers are movable, and averaging is needed to achieve super-resolution effect, so this technique is not essentially a single-shot approach. But movement of the diffusers can be done very fast, and, in principle, a super-resolution effect can be effectively achieved during the recording time of the sensor. Sun and Leith also studied the effect produced by different mismatches in the synchronized movement of the gratings/diffusers.

It was not until the beginning of the 21st century that single-shot super-resolution imaging using an off-axis holographic configuration of significant interest appeared. Mico *et al.* implemented tilted beam illumination with single-exposure capability based on the use of a VCSEL (vertical-cavity surface-emitting laser) array [147]. The VCSEL array provides a set of coherent sources that are mutually incoherent to each other. Thus, the oblique illumination stage can be easily implemented in a single shot. This approach can be viewed as the previously described Leith *et al.* approaches where there is not a spatially incoherent extended source but only a few single illumination spots covering the whole size of the extended source. Thus, each tilted beam provides a different spatial frequency slot of the input object spectrum, and all of them are reallocated to their original Fourier domain position by a set of complementary reference beams by off-axis holographic recording. The experimental layout can be seen in Fig. 14. It is a $4f$ imaging system with a limiting aperture in the Fourier plane for limiting the resolution. Figure 14(a) shows on-axis illumination, and Fig. 14(b) shows one oblique illumination beam, illustrating how additional spectral information is transmitted through the system aperture. Figure 14(c) shows experimental results presenting a high-resolution image of the object (recorded without limiting slit in the layout) in comparison to the low-resolution image shown in Fig. 14(d) as a consequence of using the slit. Figure 14(e) shows the super-resolved image when

Figure 13



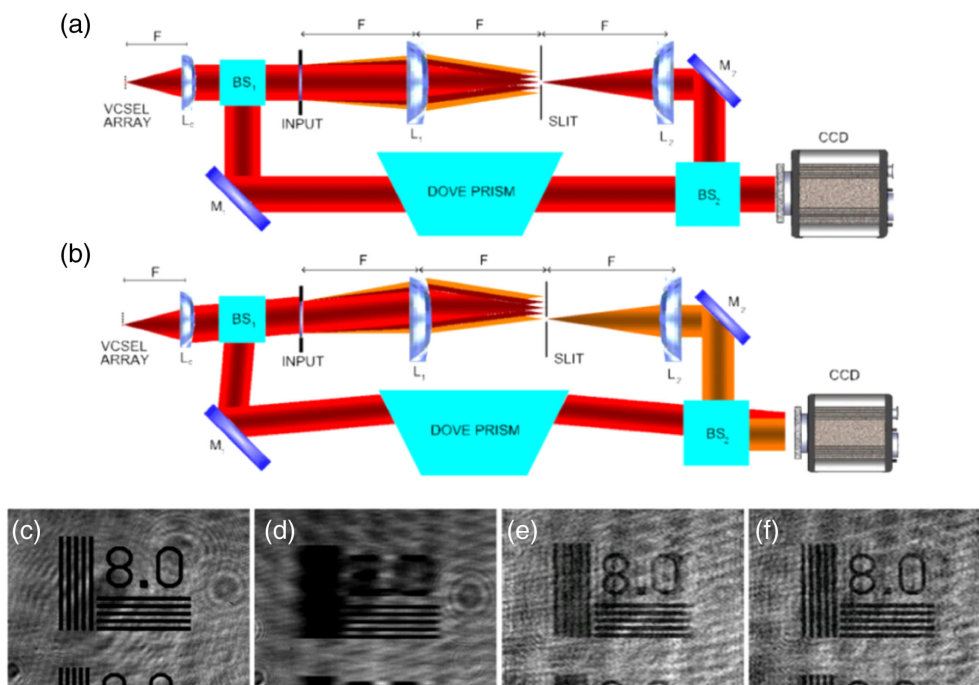
Experimental results for single-shot 1-D super-resolution by Leith *et al.* [142]. (a) Image with penalized resolution in the vertical direction and super-resolved 1-D image considering the proposed technique with (b) small and (c) large illumination sources. Figure is modified from [142].

considering three VCSEL sources generating one on-axis beam plus one tilted beam at each side. Figure 14(f) shows the super-resolved image when considering five VCSEL sources generating one on-axis plus two tilted beams at each side. Although the single-shot super-resolution effect is evident, multiplexing is done in 1-D and validated for low synthetic NA values.

These drawbacks were overcome in subsequent papers by considering higher NA values [148] and theoretically single-shot operational principles [149]. Moreover, the use of a VCSEL array for single-exposure super-resolution imaging was also extended to the field of lensless digital holography, in which the sample is imaged without lenses [150]. Also, in lensless imaging schemes, other approaches were proposed in digital holography to increase the resolution limit using a single camera snapshot. One can find modern implementations of Lukosz's original idea [144,145] where diffraction gratings (1-D and 2-D) are used to redirect additional spatial frequency information onto the digital camera sensitive area, where the extra information is retrieved by imaging the bandpass images at the Fourier domain [151–154]. In addition, the single-shot encoding illumination stage has also been proposed with coherence encoding by means of pulsed illumination [155] as well as polarization encoding [156] in digital holography to enable the super-resolution effect. Extension of this to single-exposure super-resolution digital holographic microscopy was straightforward by using coherence gating [29] and polarization encoding [157–159].

Leaving aside polarization coding, the single-shot operational principle is mainly achieved using coherence encoding whether with extended (spatially incoherent)

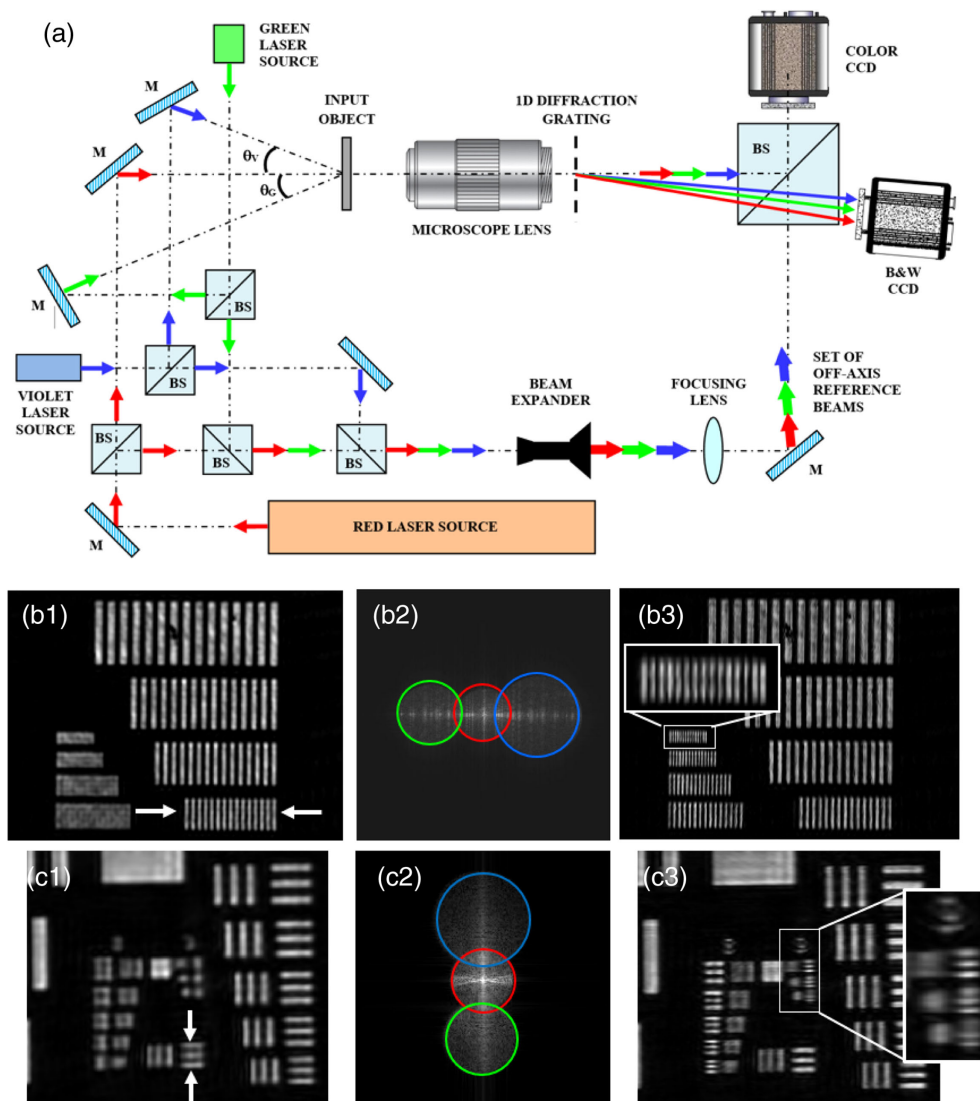
Figure 14



Approach proposed by Mico *et al.* [147] providing single-shot 1-D super-resolution imaging. The experimental layout is included in (a) and (b) for on-axis and off-axis illuminations, respectively, and the experimental results can be seen through (e) to (f) corresponding with a (e) high-resolution image (for comparison purposes), (d) low-resolution image using on-axis illumination, and (e) and (f) super-resolved image with three and five beams, respectively, using the proposed approach. Figure is modified from [147].

sources or with VCSEL arrays or using pulsed (temporally incoherent) illumination. Following in the same line, Calabuig *et al.* [160,161] reported on a method for 1-D single-exposure super-resolved interferometric microscopy (SESRIM), where the single-exposure working principle was achieved by combining angular and wavelength multiplexing incoming from a set of tilted beams of different wavelengths. The approach was validated using two different experimental configurations for the decoding stage. The first one involves a color camera where the red–green–blue (RGB) channels are tuned with the illumination beams [160]. The second one used a monochrome camera, where the separation of the information encoded in each illumination beam is performed by FOV limitation [161]. Figure 15(a) depicts an experimental layout where both approaches are included, with the only exception being the limiting slit attached to the input object for FOV restriction. In both approaches, a multiplexed off-axis hologram is recorded in a single camera snapshot coming from the incoherent addition of three individual holograms, each one of them carrying different spatial frequency information of the input object spectrum. Once

Figure 15



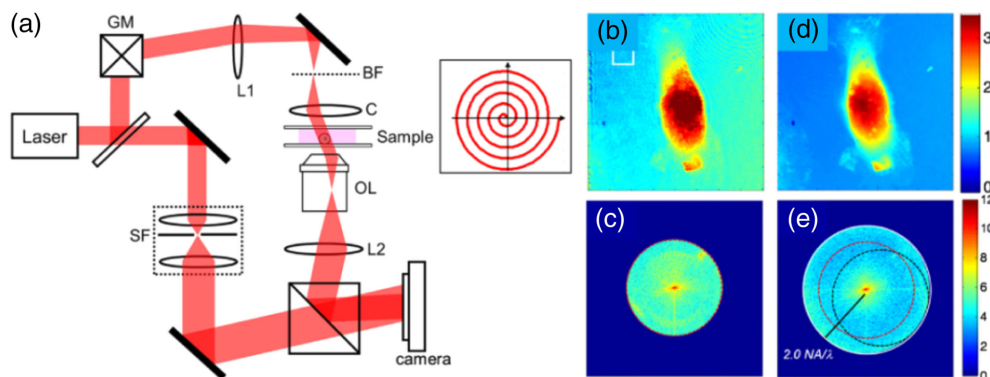
SESRIM approach reported by Calabuig *et al.* [160,161]. (a) Experimental layout of both approaches. (b) Experimental results from [160]. (c) Experimental results from [161]. Figures are modified from [160,161].

the individual complex amplitude information is retrieved, a SA is assembled, and a super-resolved image is finally obtained as the inverse Fourier transform of the information contained in the SA. Figures 15(b) and 15(c) include the experimental results from Refs. [160,161], respectively, and Figs. 15(b1) and 15(c1) show the conventional (low resolution) image without applying the proposed technique, Figs. 15(b2) and 15(c2) show the generated SA, and Figs. 15(b3) and 15(c3) show the super-resolved image. Although SESRIM was originally conceived for providing a 1-D super-resolution effect, 2-D single-shot super-resolution imaging is also possible by selective angular multiplexing. Next, the SESRIM concept was extended to the field of digital in-line holographic microscopy [162].

In addition to these single-shot techniques, super-resolution in digital off-axis holographic microscopy can also be implemented not in a single snapshot but in a fast acquisition, capable of SA generation in fractions of a second or, at least, below 1 s of total exposure time. Kim *et al.* [163] reported on a high-speed SA microscope for quantitative phase imaging of live biological cells. Using a dual-axis galvanometer-driven scanning mirror, the illumination angle can be controlled and a SA continuously generated (spiral trajectory) using 360 recorded holograms in less than one-thirteenth of a second. A phase-referencing algorithm was developed to constructively add multiple angular images for the aperture synthesis. Thus, the lateral resolution is improved because of the generated SA, and the phase sensitivity is enhanced as a consequence of the averaging between all the recorded images. Figure 16 includes the experimental setup and some of the experimental results. They used a high-NA condenser lens (1.4) in combination with a high-NA objective (1.4), and the maximum oblique beam illumination provided 0.8 NA, so that the generated synthetic NA reached the maximum value (2.0 NA).

This layout was also lately validated in tomographic phase microscopy, as discussed in Section 7 of the present paper, for fast (less than 1 s) refractive index imaging of cellular organelles in HeLa, HT-29, and T84 cells [164,165]; for high-contrast 3-D DIC (differential interference contrast) imaging of live biological cells [166]; to measure the growth of mammalian cells accurately [167]; and for further improvement for real-time reconstruction of dynamic 3-D refractive index maps of individual cells via optical diffraction tomography [168]. Nowadays, tomographic diffractive microscopy is an open field performing fast and real-time imaging on biosamples [169–171].

Figure 16

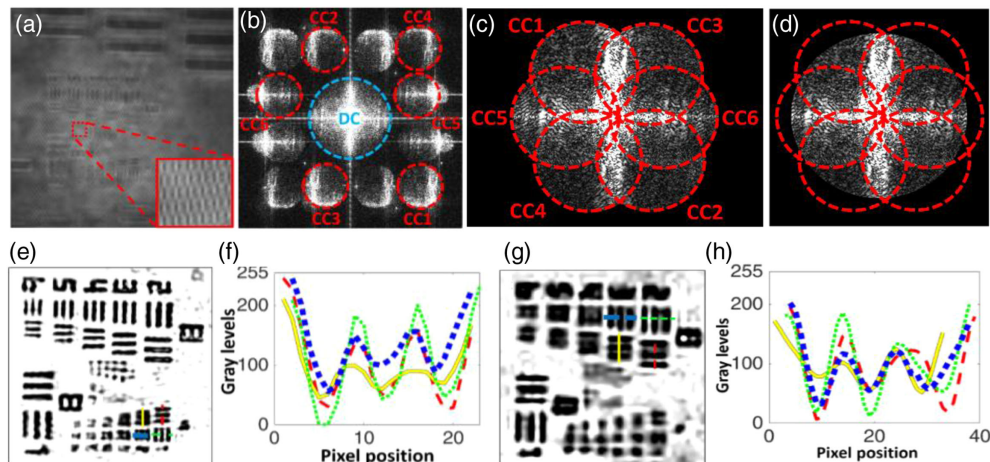


High-speed synthetic aperture microscopy. (a) Experimental layout. (b)–(e) Imaging a live microglia cell: (b) and (c) the conventional image and aperture, respectively; (d) and (e) the super-resolved and synthetic aperture, respectively. Figure is modified from [163].

Mirsky and Shaked [28] have lately presented the first experimental realization of 6PH, an off-axis interferometric system capable of spatially multiplexing six complex wavefronts while using the same number of camera pixels needed for a single off-axis hologram. They used the holographic encoding shown in Figs. 2(d) and 3, such that each of the six parallel complex wavefronts is encoded using a different fringe orientation and can be fully reconstructed. In this paper, they utilized 6PH to increase resolution in dynamic SA imaging, where each of the six optically compressed off-axis holograms encodes a different spatial frequency range of the imaged sample.

This 6PH system is based on a modified Mach–Zehnder interferometer illuminated by a partially coherent light, which is split into six parallel channels using a 2-D diffraction grating. A phase delay plate of a different thickness is used in each of the six channels that illuminate the sample at different angles, to image different spatial frequency contents from the sample. The sample beams are unified with the matching reference beams, which went through phase delay plates with matching thicknesses, and each channel creates off-axis interference fringes of a different orientation on the camera, such that nonmatching beams do not interfere with each other, and maximum usage of the spatial frequency domain is obtained. The six-pack hologram of a 1951 USAF test target, acquired in a single camera exposure, and its 2-D Fourier transform are shown in Figs. 17(a) and 17(b), respectively. The CC term positioning when creating the SA, and the final cropped SA (for isotropic frequency distribution), is shown in Figs. 17(c) and 17(d). The reconstructed amplitude image obtained after performing an inverse Fourier transform is shown in Fig. 17(e), and Fig. 17(f) shows the cross-sections along the marked lines at the bottom of Fig. 17(e). For comparison, the same test target was imaged by the system using a normal-incidence illumination beam and a single reference beam to provide a standard off-axis hologram [see Figs. 17(g) and 17(h)]. The approximate increase in resolution is between 1.58–1.78

Figure 17



Simultaneous synthetic aperture super-resolution imaging based on 6PH. (a) Six-pack multiplexed hologram of a USAF target, experimentally acquired in a single camera exposure. Inset shows fringes magnified five times. (b) The corresponding spatial frequency power spectrum. (c) Positioning of CC terms in the synthetic aperture. (d) Same synthetic aperture as in (c) after cropping to the largest possible circle. (e) Amplitude image produced from (d). (f) Profiles along the lines marked in (e) demonstrating the smallest resolvable elements. (g) and (h) Results obtained from a standard off-axis hologram, for comparison to (e) and (f). Figure is modified from [28].

times the original resolution, corresponding to NAs of 0.395–0.445. This closely matches the expected increase in resolution, which was calculated to be 1.62 times. This technique is especially useful for dynamic samples, as it allows the acquisition of six complex wavefronts simultaneously. Additional experimental demonstrations provided in this paper include using 6PH to image dynamic samples such as a moving 1951 USAF test target, flowing red blood cells, and flowing polymer beads of 1 μm in diameter.

7. ANGULAR MULTIPLEXING FOR TOMOGRAPHY

Off-axis holographic multiplexing can be used to increase the acquisition rate in holographic tomography (HT). In contrast to regular digital holography that provides OPD (optical path delay) topographic maps without sectioning capability for objects that are dense on the z axis, HT provides the 3-D refractive index distribution within weakly scattering objects without labeling, which corresponds to the internal structure of cells and tissues, as long as distinctive refractive indices are present. This is especially useful in medical diagnosis and biological research [172]. HT requires capturing holograms of the object from several viewing directions, and relies on the theory first developed by Wolf [173]. Off-axis holograms captured at different illumination directions contain information on the field illuminating the object (plane, monochromatic wave $U^{(i)}(\mathbf{R})$) and scattered from the object ($U^{(s)}(\mathbf{R})$), which, at the point defined by position vector \mathbf{R} in three-dimensional (3-D) space, can be defined by

$$U(\mathbf{R}) = U^{(i)}(\mathbf{R}) + U^{(s)}(\mathbf{R}). \quad (6)$$

The equation for the optical field obeys the following wave equation:

$$(\nabla^2 + k_0^2)U^{(s)}(\mathbf{R}) = F(\mathbf{R})U(\mathbf{R}), \quad (7)$$

where $F(\mathbf{R})$ is the scattering potential of the object with respect to its surrounding medium, which can be found as follows:

$$F(\mathbf{R}) = -k_0^2[n^2(\mathbf{R}) - 1], \quad (8)$$

in which k_0 is the wave vector $k_0 = 2\pi/\lambda_0$ and $n(\mathbf{R})$ is the refractive index function in object space.

To capture HT, regular holographic setups need to be equipped with additional hardware [174] that enables tomography by either rotating the sample or changing the illumination direction. Object-rotation configuration enables full-angle tomography, while illumination rotation configuration leads to limited-angle tomography. Depending on the configuration used and taking into account optical diffraction, the complex amplitudes of the scattered field are mapped in the 3-D Fourier spectrum of the object on caps of Ewald spheres that are located in different manners [175]. This leads to different spatial frequency coverage and either almost isotropic resolution for full-angle tomography or highly anisotropic resolution with improved transverse resolution at the expense of axial resolving capability for limited-angle tomography. In order to mitigate the lack of information in limited-angle tomography, an iterative Gerchberg–Papoulis algorithm can be used, during which a nonnegativity constraint is applied [174].

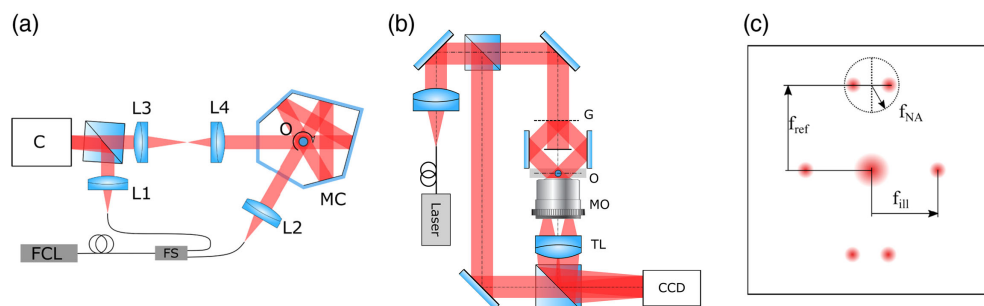
The common denominator of the aforementioned configurations is the necessity of acquiring data sequentially in time. This limits the applicability of HT to quasi-static samples especially in the case of biological applications. The slowest approach is the

object-rotation configuration, since the object rotated should not tumble during the measurement (e.g., when rotated inside a fiber capillary [176,177]). Illumination scanning HT systems have much greater potential for shortening the acquisition time by using galvanometer mirrors and a fast camera [178], or avoiding mechanical scanning by using a SLM, such as a digital micromirror device (DMD) [179]. Decreasing measurement time is also realized by data sparsification, i.e., acquiring fewer projections [179,180], which can only be applied when a powerful and more computationally demanding reconstruction algorithm [174], e.g., based on compressed sensing [181], is used. The alternative solution is to acquire more than one projection at a time. This idea has been first employed in x-ray computed tomography (CT), in which the source and detector revolve around the measured object. In the case of x-ray CT, multiple sources and detectors are available, which reduces the number of angular positions required for a full scan [182,183]. This would ultimately lead to instantaneously obtaining a sparse dataset [184]. Furthermore, it is also worth noting that the general idea of multiplexing projections with multiple imaging systems in tomography has also been demonstrated for optical projection tomography [185]. In HT, however, the idea of applying multiplexing appears to have been developed independently and stems from holographic data storage concepts of angular multiplexing [186,187].

Regardless of the system configuration, the practical implementations of angular multiplexing techniques for tomography usually require one of the following components: (a) diffraction grating and/or mirrors [188–191]; (b) SLM [192–194]; (c) microlens array [195]; (d) diffractive beam splitter.

One of the first multiplexed HT systems was based on an object-rotation-configuration and presented in Ref. [188], as shown in Fig. 18(a). In this work, a mirror system, which may be placed around the rotated object, was designed. This would cause the illuminating beam to pass through the sample more than once before entering the microscope objective. To recover the projections, it would be necessary to propagate the complex optical field to a set of axial locations. In this work, however, the influence of the diffraction was not taken into account, and the overlapping scattered waves were the major source of error, which prevented the authors from

Figure 18



(a) Multimirror object cuvette, which enables illumination direction multiplexing in object-rotation HT. Figure is modified from [188]. L1, L2, collimators; MC, multimirror cuvette; L3–L4, imaging system; O, rotated object. (b) Object-rotation configuration in holographic tomography with two multiplexed views. G, diffraction grating; O, object placed in a rotary fiber cuvette; MO, microscope objective; TL, tube lens; CCD, camera. (c) Spectrum of a hologram obtained in a multiplexed object-rotation HT system; f_{NA} , frequency region corresponding to the NA diameter; f_{ref} , frequency corresponding to reference beam angle; f_{ill} , frequency corresponding to the angle between illumination beams. Figure is modified from [190].

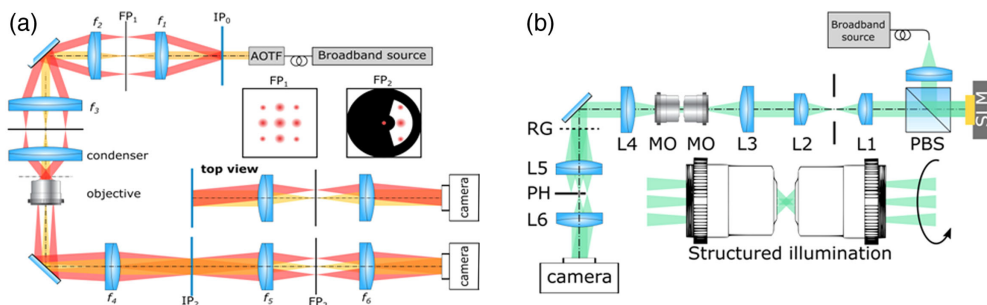
using the full potential of the technique—only two projections were acquired in a single hologram. A similar idea of using a mirror to assist tomography was presented by Mudry *et al.* [189]. In this work, the mirror was placed right behind the sample to obtain a field reflected off the sample and reflected off the back of the sample, thus multiplexing two projections.

The second object-rotation HT work, which benefited from holographic multiplexing, was presented in Ref. [190]. Here, the authors used structured illumination for an object measured in a Mach–Zehnder-based digital holographic setup. The biological sample was inserted inside a hollow-core fiber capillary and rotated to obtain projections. In the sample beam, a diffraction grating and two mirrors were placed, as demonstrated in Fig. 18(b). This provided two illumination directions for a single hologram. The reference beam was tilted in a plane perpendicular to the one containing the sample beams and resulted in the spectrum shown in Fig. 18(c). The waves scattered on the sample overlapped in the Fourier domain, degrading the quality of the retrieved complex amplitudes. What is more, the need to filter a smaller area within the NA region in the frequency domain [f_{NA} in Fig. 18(c)] also limited the resolution of the technique.

A similar concept of multiplexing angular illuminations into a single hologram, generated with a diffraction grating, was introduced by Hosseini *et al.* [191]. In this approach, the system was built as a common-path digital holographic setup, as demonstrated in Fig. 19(a). The source used was a broadband 400–700 nm supercontinuum source, coupled to an acousto-optic tunable filter (bandwidth of 2–7 nm). Changing the wavelength results in a change of Ewald's sphere radius in the 3-D Fourier spectrum of the reconstructed object. Such wavelength scanning fills in a certain portion of the spectrum; however, it is not sufficient for a successful reconstruction. The authors used a diffraction grating placed in plane IP_0 , conjugate to the sample and camera planes, to provide three multiplexed illumination directions and, thus, reduce the measurement time. The reference beam was generated by placing a spatial filter in plane FP_2 . In this case, again, the spatial frequencies, which overlapped in the frequency domain, were not fully de-multiplexed in the full NA region of each projection.

When using a typical measurement system for HT, based on mechanical scanning of the illumination, it is not possible to generate multiple illumination angles without additional components, contrary to systems that use SLMs for scanning, such as a

Figure 19



(a) Wavelength scanning holographic tomography with three multiplexed fields of view. Broadband source, 400–700 nm supercontinuum; AOTF, acousto-optic tunable filter; f_1 – f_6 , lenses; IP , image-conjugate plane; FP , Fourier plane. Figure is modified from [191]. (b) Structured illumination optical diffraction tomography; broadband source, $\Delta\lambda = 30$ nm; L_1 – L_6 , lenses; MO , microscope objective; RG , Ronchi grating; PH , pinhole. Figure is modified from [192].

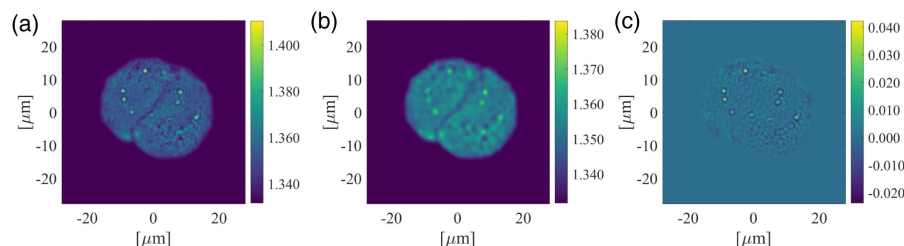
phase-only liquid crystal on silicon SLM [192,193,196] or a DMD [179,194]. In the latter, all instrumentation, required to generate multiplexed projections, is already present. What is more, due to the fact that the modulators are active components, it is possible to de-multiplex the full information from the NA area in the spectrum by sequentially shifting the phase of the illuminating beams [192–194].

One such approach, described in Ref. [192], is demonstrated in Fig. 19(b). In this case, a broadband source ($\lambda = 488 \pm 15$ nm) was used in a common-path interferometric configuration, as enabled by a Ronchi grating and a pinhole. Illumination scanning HT was realized by conjugating the SLM plane to the sample and camera planes. The aim of this work was to make HT more suitable for coupling with structured illumination fluorescence super-resolution, and did not actually focus on using multiplexing to reduce the measurement time. In this case, to retrieve the information in the full NA, the number of required phase-shifted holograms is equal to the number of illumination directions present in the multiplexed hologram. Another work, which focused on multiplexing interferometric projections with full de-multiplexing of the NA region in the spectrum, was carried out by Lee *et al.* [194], where a DMD modulator was used. The multiplexing was performed during the camera exposure due to the binary character of the scanning component. In this case, the goal of angular multiplexing of the projections was to reduce the number of diffraction-related artifacts present in the reconstructions resulting from periodic structure of the modulator. The idea of multiplexing several projections using a DMD modulator was also implemented by He *et al.* [197]. In that case, there were four projections multiplexed in a single frame without any additional de-multiplexing apart from extracting overlapped frequencies from the Fourier spectrum.

This leads to a possibility of reducing the measurement time required to obtain the full projection set for tomographic reconstruction, where the scattered fields coming from two or more illumination directions overlap in the spectrum. This overlap might degrade the quality of each retrieved projection; furthermore, the effective NA of each projection is reduced due to masking, as shown in Fig. 18(c). It may be assumed that for a weakly scattering object and a few projections per hologram, the reduced NA is more dominant in the projections than the overlapping-related artifacts, as shown in Fig. 20 [198].

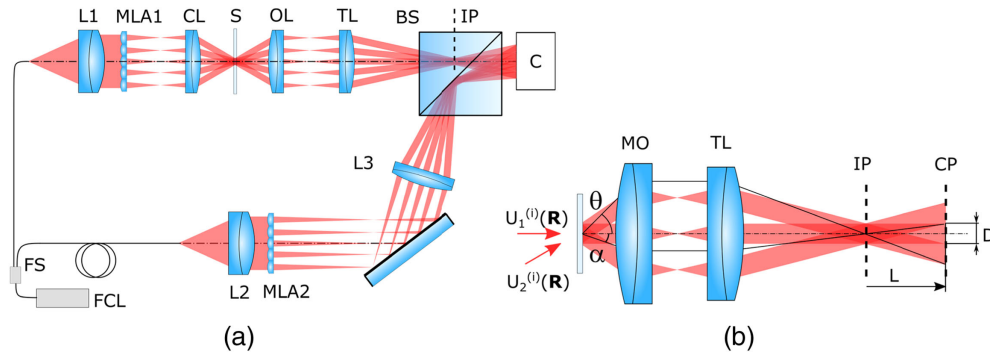
An optical system, which resembles the concept of integral imaging, was presented by Sung [195]. In this system, the multiplexed illumination directions were generated with a microlens array as shown in Fig. 21(a). The concept was based on two arrays—one to generate multiplexed projections and the second to provide a set of reference

Figure 20



$X - Y$ cross sections through the 3-D refractive index map of two HaCaT cells. (a) HT reconstruction based on 180 projections without multiplexing (ground truth); (b) HT reconstruction from multiplexing 18 holograms with 10 projections per hologram and NA masking during de-multiplexing; (c) error map calculated as a difference between (a) and (b). Figure is modified from [198].

Figure 21



Snapshot holographic optical tomography system [195]. (a) FCL, fiber-coupled laser source; FS, 2×2 fiber-optic splitter; L1, L2, L3, lenses; MLA1, MLA2, microlens arrays; CL, condenser lens; OL, microscope objective lens; TL, tube lens; BS, beam splitter cube; C, camera; (b) MO, microscope objective; CP, camera plane. Figure is modified from [195].

beams. However, the incident waves overlap when acquired in the image plane IP conjugate to sample S in the same manner as for previously described cases (Figs. 18 and 19). To avoid the overlap of the $U^{(i)}(\mathbf{R})$ waves, the magnification of the OL-TL system and the camera position may be matched with an additional $4f$ system, so that the waves are fully separated after distance L in the camera plane CP as demonstrated in Fig. 21(b). The retrieved complex amplitudes are then propagated to the image plane by using the angular spectrum method. However, such an approach does not address the fact that each incident $U^{(i)}(\mathbf{R})$ wave generates a scattered wave $U^{(s)}(\mathbf{R})$, which fills the entire NA of the imaging system within angle θ in Fig. 21(b). While masking a single camera segment D , corresponding to a single $U^{(i)}(\mathbf{R})$ wave, limits the NA of the projection to $\text{NA} = n \sin \alpha$ instead of $\text{NA} = n \sin \theta$, and the detrimental influence of scattered fields resulting from other incident fields is not mitigated.

To sum up, the existing solutions for multiplexed illumination angles in tomography may be divided into four groups depending on the spatial frequency overlap, separation, and de-multiplexing: (a) frequency overlap [190,191,197,198]; (b) frequency overlap and full de-multiplexing [189,192,194]; (c) frequency overlap and spatial separation [195]; (d) projections separated in frequency domain (full de-multiplexing). So far, the only solution exhibiting the potential for full separation of the projections is to use coherence gating [29] to separately detect the scattered fields in the spectrum as in the six-pack off-axis holography [28] used for super-resolution and apply this technique to HT with illumination scanning (see Section 6).

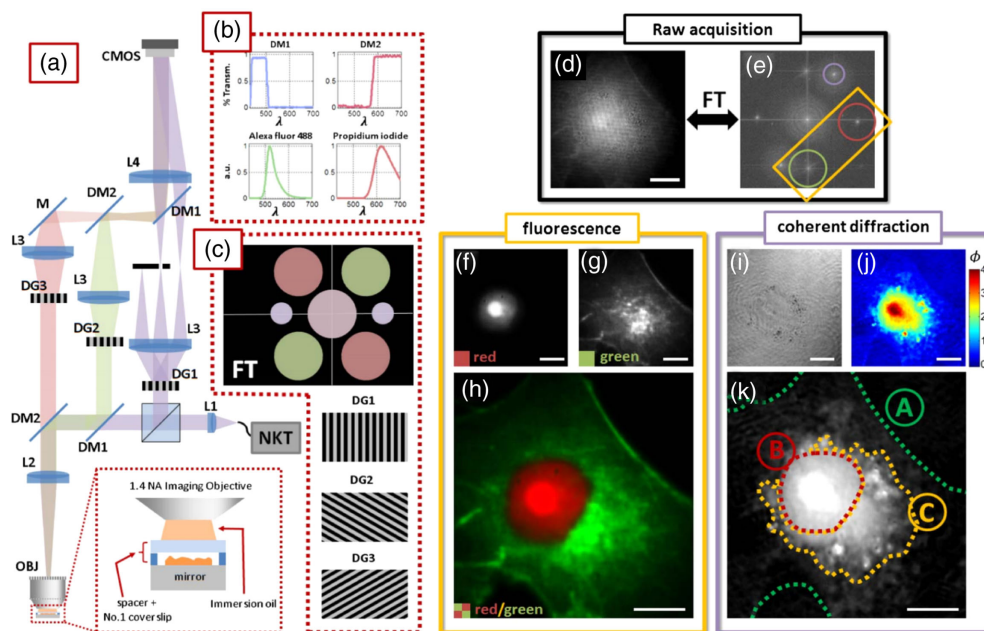
Dardikman *et al.* [199] have used angular off-axis holographic multiplexing to obtain four-dimensional phase unwrapping for time-lapse quantitative phase microscopy. This technique allows reconstruction of optically thick objects that are optically thin in a certain temporal point and angular view. This approach is also useful for time-lapse HT, where the use of the angular dimension may allow solving of phase ambiguities for angular views that could not be solved using the spatial and temporal dimensions alone.

8. MULTIPLEXING QUANTITATIVE PHASE IMAGES WITH FLUORESCENCE

Multiplexing of off-axis holography with fluorescence is another possible multiplexing application. Holography provides the quantitative phase profile without labeling, but does not have molecular specificity, e.g., we cannot be sure where the nucleus

of the imaged cell is, since its boundaries are not distinguishable by its OPD profile alone. On the other hand, fluorescent microscopy can label certain cell organelles, but is not fully quantitative, since it is hard to interpret the gray level values in the image obtained in terms of meaningful physical measurements. Thus, simultaneous acquisition of holographic and fluorescent channels is advantageous for dynamic samples that do not allow sequential acquisition, but still require both the quantitative phase imaging provided by holography and the molecular specificity provided by fluorescence. Normally, any incoherent illumination of the sample or emission from the sample, such as white light or fluorescence, respectively, would overlap with the DC term in the spatial frequency domain of the hologram. On the other hand, if a white light holographic setup is used, it is possible to create an off-axis hologram from the fluorescent channel as well [200–203]. Specifically, in the setup presented in Ref. [204], white light diffraction phase microscopes were combined, so that it was possible to multiplex two fluorescent off-axis holographic channels and one regular off-axis holographic channel for quantitative phase imaging. The combined microscope output of fluorescent emission and laser transmission from the sample are passed to a diffraction grating. This results in a first-order beam that travels along the optical axis and continues through a $4f$ system of two converging lenses to produce

Figure 22

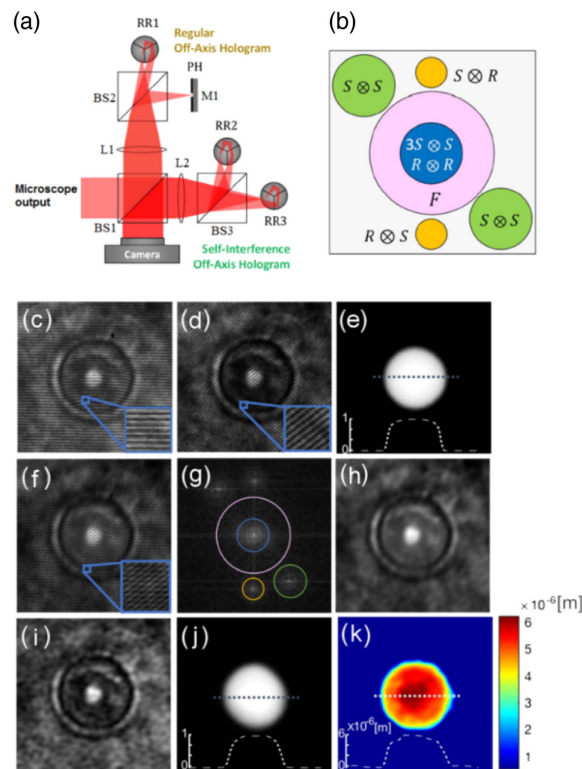


Multiplexed holography/fluorescent microscopy: (a) optical schematic for the multiplexed microscopy system with red–green–blue color codes for the separate optical arms and associated signal. (b) Spectra for dichroic mirrors used in system and fluorophores used for cell imaging. (c) Example of Fourier separation between microscope's fluorescent and coherent signals (color coded) using rotated gratings DG1, DG2, and DG3. Experimental results when imaging a biological cell: (d) raw acquisition and (e) associated Fourier spectrum. Digital filters used for fluorescence and QP reconstructions are shown. Fluorescence reconstructions from the (f) red and (g) green channels, showing nucleus and *F*-actin, respectively. (h) Red/green fluorescence channel overlay. (i) Amplitude and (j) quantitative phase image reconstructions are also shown. (k) Gray-scale quantitative phase image with labeled cell body, nucleus, and potential endoplasmic reticulum is shown. Scale bar corresponds to $10\ \mu\text{m}$. Figure is modified from [204].

the fluorescence holograms and the regular hologram on the camera simultaneously. The zeroth-order beam, which is traveling at an off-axis angle, enters the first lens of the $4f$ system, and is then spatially filtered by a pinhole in the Fourier plane, creating a clean reference beam. Figures 22(a)–22(c) present the holographic setup, with the spectra of its dichroic mirrors and a schematic drawing of the spatial power spectrum of the multiplexed hologram, and Figs. 22(d)–22(k) show selected results.

Another technique for multiplexing a hologram with fluorescence is illustrated in Fig. 23(a) [205]. In this technique, the holographic DC term is measured by an additional off-axis holographic channel, and therefore it can be subtracted from the sample off-axis hologram and leave space in the spatial frequency domain for the fluorescent signal. In the system depicted in this figure, beam splitter BS1 splits the combined output beam of the microscope. The first of the split beams is then directed into a module similar to the IDIA module discussed earlier. In this module, the beam passes through lens L1 and is split again by beam splitter BS2, with one beam being shifted off the optical axis and reflected back by retro-reflector mirror RR1, while the other beam is spatially filtered and reflected back by a mirror-mounted pinhole, PH and M1. These beams then travel back through BS2, L1, and BS1 and produce an off-axis hologram on the camera. The second beam that was split from BS1 passes through lens L2 and is then split by beam splitter BS3. Each of these beams are shifted off the optical axis and reflected back by retro-reflector mirrors RR2 and RR3, respectively. These beams then travel back through BS3, L2, and BS1 to produce an off-axis hologram between two identical sample beams. The three sample beams also contain the fluorescence and form the fluorescence image on the camera. The beams from BS2 do

Figure 23



Multiplexed holography/fluorescent microscopy: (a) external off-axis holography and fluorescence multiplexing system. BS1–BS3, beam splitters; L1–L2, lenses; M1, mirror; PH, pinhole; RR1–RR3, three-mirror retroreflectors. (b) Diagram of the spatial frequency power spectrum. Figure is modified from [205].

not interfere with the beams from BS3 as the laser used has a short coherence length and the optical path lengths of these sets of beams are not equal. The spatial frequency power spectrum of the multiplexed hologram is illustrated in Fig. 23(b), where it can be seen that there are two off-axis hologram CC terms, $S \otimes R$ and $S \otimes S$, with $S \otimes R$ being the normal off-axis hologram CC term and $S \otimes S$ being the self-interference hologram CC term. Using the information from the self-interference hologram as well a reference hologram captured without a sample, the DC term can be deleted from the multiplexed hologram by subtraction, rendering F , the spatial frequencies of the fluorescence image, free of any unwanted additional frequencies. Experimental results for imaging a fluorescent microbead are given in Figs. 23(c)–23(k).

9. MULTIPLEXING FAST EVENTS

An intriguing application of off-axis multiplexing is the holographic recording of fast events [89,204–209]. By illuminating the sample with ultrashort laser pulses over a timespan shorter than the exposure time of the digital camera, each pulse forms a separate hologram of the sample in the single exposure, with each hologram corresponding to a single pulse, and thus, a single time instance. This effect is achieved by splitting a single laser pulse into a number of sample pulses and an equal number of reference pulses. By carefully matching the optical path length that each sample and reference pulse pair travel, the pulse pairs are made to meet again at the camera plane at precisely the same time. As the sample-reference pulse pairs are sequential, each sample pulse only interferes with its reference pulse. Each of the pulses, as well as the time interval between them, can be designed to be just femtoseconds long; thus, the multiplexed holograms will each be different snapshots of the sample over a very short time period. This technique has been used to examine fast events such as air discharge events [204], laser-induced ionization of air [205,206] (see experimental system and results in Fig. 24), light pulse field propagation [207], pulsed laser ablation of a solid surface [208], propagation of a crack in a sample [209], and sample deformation [89]. Recently, multiple ultrafast pulses interfered with a chirped reference pulse, and were used to reconstruct optical wavefronts at different times encoded into the hologram [210,211].

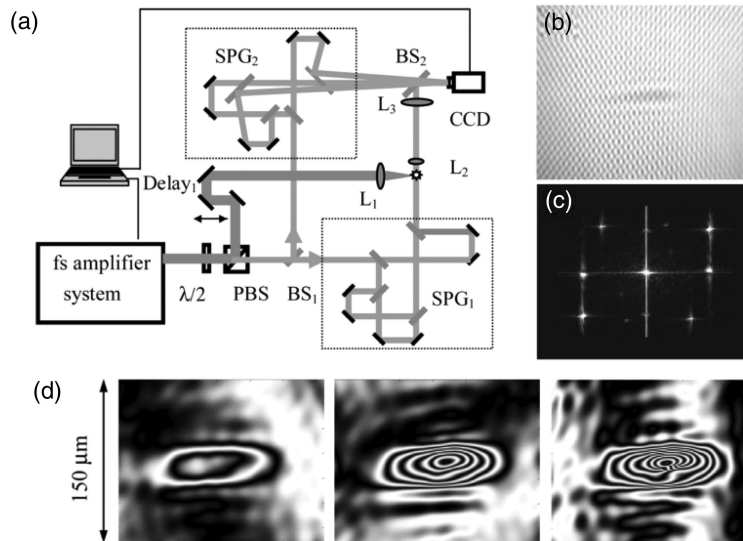
10. MULTIPLEXING FOR POLARIZATION MEASUREMENTS

Holographic multiplexing can also be used for polarization state, Jones, and Stokes matrix extraction [212–220]. Some samples may change the polarization of the illuminating light wave, may be birefringent, or may absorb different amounts of light depending on the polarization orientation, a property known as diattenuation. By illuminating the sample with circularly polarized light and interfering the sample beam with two linearly and orthogonally polarized reference beams, the birefringence retardation and axis orientation of each point in the sample can be extracted from the two multiplexed holograms [217]. To take this idea further, by illuminating the sample with two linearly and orthogonally polarized beams and interfering each of these sample beams with two linearly and orthogonally polarized reference beams, in which the two reference beams are polarized at an angle of -45° and 45° relative their sample beam polarization, the final multiplexed hologram will contain four complex wavefronts of the sample, each providing unique data on the polarizing nature of the sample. Using this polarization data, it is then possible to extract the four parameters of the Jones matrix, which details the polarizing, birefringence, and diattenuation characteristics of an optical element, for each point in the sample [218]. The proposed system, shown in Fig. 25(a), is based on a Mach–Zehnder interferometer integrating two mutually incoherent sources S1 and S2, each of which passes through a 2-D

orthogonal grating, G1 or G2, and is then split by polarized beam splitter PBS to a sample beam and a reference beam. In the sample path, only the zero diffraction orders from G1 and G2 pass through the pinhole filter PF1 and illuminate the sample S with two orthogonal polarization states, horizontal (A1) and vertical (A2).

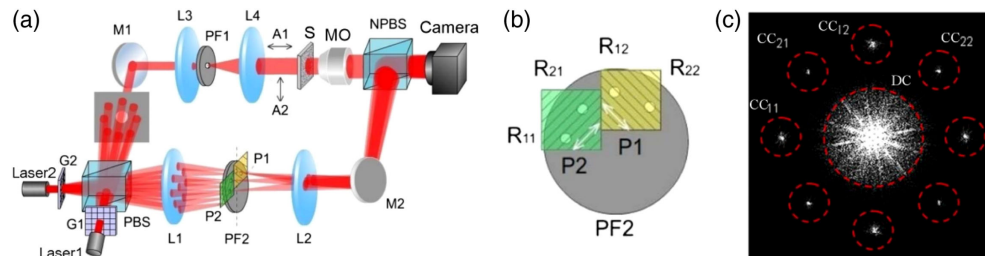
In the reference path, the zero diffraction orders from G1 and G2 are blocked, and four of the first diffraction orders pass through the four-pin-hole spatial filter PF2 as the reference beams. This creates on the camera a multiplexed hologram created by four different-orientation off-axis interferences. The orientation of G2 is set at 45° relative

Figure 24



(a) Pulsed digital holographic microscopy system with spatial angular multiplexing of rapid events. SPG, subpulse generator; BS, beam splitter; PBS, polarizing beam splitter. (b) The multiplexed hologram composed of three overlapped sub-holograms while recording air ionization. (c) The corresponding spatial frequency domain of the multiplexed hologram. (d) Counter maps of the phase differences during the air-ionization process, time resolution of 50 fs, and frame interval of 300 fs. Figure is modified from [205,206].

Figure 25



(a) Schematic illustration of a one-step Jones matrix polarization holography system. (b) Four-pin-hole spatial filter PF2, with orthogonal linear polarizers, P1 and P2, attached. (c) Spatial frequency domain of a four-channel multiplexed hologram. Laser1, Laser2, laser sources; G1, G2, diffraction gratings; M1, M2, mirrors; L1–L4, lenses; S, sample; MO, microscope objective; A1, A2, orthogonal polarization states. The cropped CC terms are processed to extract the full Jones matrix parameters. Figure is modified from [218].

to G1, and the four pinholes on PF2 are located as shown in Fig. 25(b). Two orthogonal linear polarizers P1 and P2 are attached behind the pinholes, so that the reference components R11 and R21 are linearly polarized along 45° , with respect to vertical axis, whereas R12 and R22 are transformed into linearly polarized beams orientated at -45° . After acquiring the multiplexed hologram in a single camera exposure, the four CC terms—CC11, CC12, CC21, and CC22 are then cropped from the spatial frequency domain of the multiplexed hologram [shown in Fig. 25(c)], are inversely transformed back to the spatial domain, and can be processed to extract the full Jones matrix parameters of the sample S (see details in Ref. [218]).

11. DIGITAL MULTIPLEXING FOR RAPID WAVEFRONT RETRIEVAL

Off-axis holographic multiplexing can be implemented optically, thus by projecting several off-axis holograms on the camera at once (as presented in Sections 3–10). Still, another way is to implement off-axis holographic multiplexing digitally [32,49,221–227]. This means taking several experimentally acquired regular (not multiplexed) off-axis holograms, rotating them in the computer, and summing them into a multiplexed hologram (or positioning the wavefront matrix in the spatial frequency domain matrix without overlap to generate the multiplexed hologram matrix). This can be useful for rapid wavefront extraction [49,221–224], compression of off-axis holograms [225,226], or for visualization purposes, when the hologram displaying device is slower than the camera acquiring the holograms [32]. Digital multiplexing of hundreds of computer-generated holograms can also be performed, e.g., for beam shaping [227]. However, in this case, the input holograms are not acquired optically first, but rather generated digitally.

In contrast to optical multiplexing of off-axis holograms, where multiple off-axis holograms are projected onto the camera at once, in digital multiplexing, there is no problem with sharing the dynamic range of the camera or with the possibility of unwanted cross terms in the spatial frequency domain. In Refs. [221,223], six algorithms for rapid retrieval of the complex wavefront from a sequence of regular off-axis holograms were introduced. Algorithm B [221] is a basic algorithm, and does not include multiplexing, but rather only a 2-D Fourier transform for each off-axis hologram in the sequence, followed by cropping the CC term and applying an inverse 2-D Fourier transform, followed by phase extraction and unwrapping (see Fig. 26).

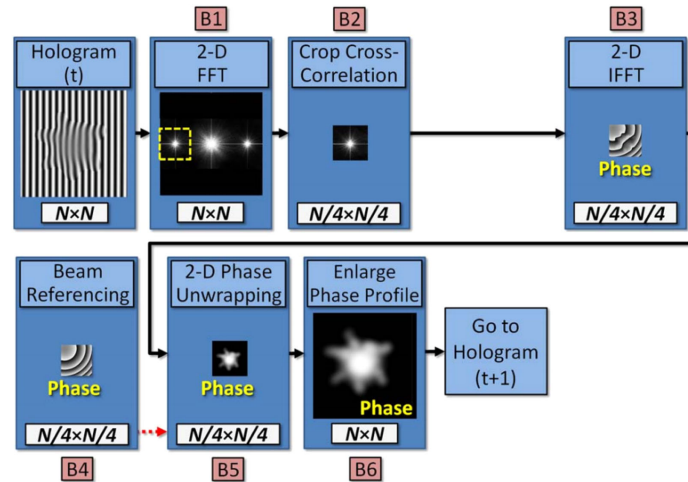
Algorithm C [221], shown in Fig. 27, multiplexes two holograms by summing one hologram with another one which is 90° rotated, before applying a single 2-D DFT to extract both CC terms. This lets us access the Fourier space in a single 2-D Fourier transform, thus saving computation time when extracting the complex wavefront.

Algorithm D [223] multiplexes four holograms by placing two 90° rotated holograms in the real part of a synthetic hologram and an additional two in its imaginary part, prior to applying a single 2-D Fourier transform for all four holograms. The SM algorithm [222] also multiplexes four holograms into a single complex hologram, by multiplying each hologram with a tilted plane wave, and performing 1-D Fourier transform on the rows followed by 1-D Fourier transform on only one-quarter of the columns, creating an effective 1.25 Fourier transform.

Algorithm E [223] is similar to Algorithm B, except that it resamples the rows four times prior to applying 1-D Fourier transform on the rows only. Algorithm F [223] is a combination of Algorithms D and E, storing one resampled hologram in the real part of a synthetic complex hologram, and a second hologram in its imaginary part. The CSM algorithm [224] is a combination of the SM algorithm and Algorithm D, multiplexing eight holograms into a single complex hologram by creating four pairs

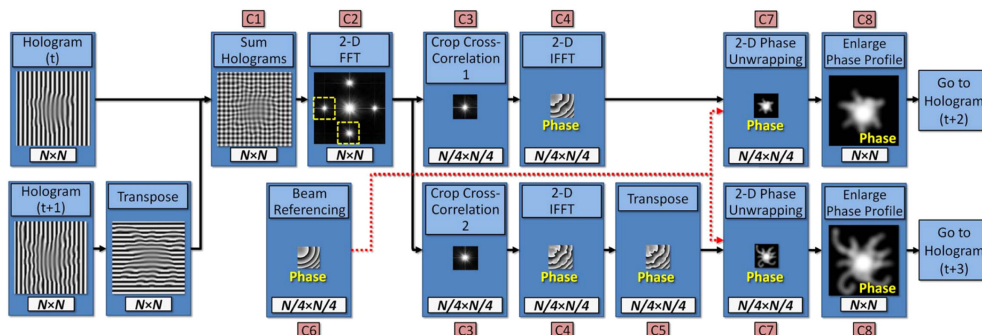
of complex holograms and multiplying each pair with a tilted plane wave. Algorithms G–J are presented in [37]. Here, there is use of optimal spatial multiplexing of off-axis holograms to fill the entire spatial frequency domain, including the space previously occupied by the intensity of the sample. This approach enables spatial digital compression of eight off-axis holograms into a single real-valued multiplexed hologram, having the same number of pixels as each of the input holograms. Since the output multiplexed hologram contains only real values, it can be used for rapid display of eight wavefront reconstructions at once, which is useful for real-time visualization, when the hologram display device is slower than the acquiring camera. Next, Ref. [37] presented a further generalization of this technique to digital multiplexing of 16 real-valued holograms into a single complex-valued hologram by simple arithmetic operations in the hologram domain. Then, the extraction of the 16 wavefronts includes a single 2-D DFT to access the spatial frequency domain, allowing fast reconstruction, which is useful for real-time processing of off-axis holograms, with improved processing rate compared to current hologram processing algorithms. A comparison between the run times of all these algorithms was implemented in Ref. [37], where all algorithms were implemented in the most efficient way possible

Figure 26



Algorithm B (conventional off-axis holography phase extraction algorithm), cropped cross-correlation algorithm for extracting quantitative phase profiles from off-axis holograms. Figure is modified from [221].

Figure 27



Algorithm C, digital off-axis hologram multiplexing algorithm for extraction of the quantitative phase profiles from off-axis holograms. Figure is modified from [221].

Table 2. Comparison between Various Phase Retrieval Algorithms^{a,b,c,d}

Algorithm	128	192	256	320	384	448	512	MSE
B [221]	1799	953.7	624.5	375.0	292.8	215.0	145.0	0.058
C [221]	2089	1119	728.8	478.2	339.6	245.4	173.4	0.085
SM [222]	2044	1234	719.6	488.1	335.7	247.4	185.9	0.065
D [223]	1991	1068	719.6	482.4	323.5	248.6	175.8	0.085
E [223]	913.7	694.4	546.4	457.0	382.9	319.1	251.1	0.345
F [223]	1301	912.2	691.7	555.8	434.4	341.9	247.4	0.066
CSM [224]	2040	1120	707.9	484.1	348.4	254.1	181.5	0.106
G [37]	2182	1201	727.7	489.6	349.6	255.3	185.3	0.043
H [37]	1446	1021	716.1	547.9	428.6	346.2	249.6	0.100
I [37]	1986	1113	672.3	467.4	335.4	240.6	171.2	0.054
J [37]	1573	1073	736.9	545.8	442.7	329.9	247.0	0.079

^aThe reconstruction rate is given in fps for various square input hologram sizes after being averaged over 1200 reconstructions.

^bThe last column shows the MSE in rad² for the 512 × 512 input, averaged over nine simulated phase images.

^cThe best result in each column is highlighted.

^dTable is modified from [37].

and on the same computer platform to allow a fair comparison. The full details of Algorithms A–J are given in Refs. [37,221,223].

As shown in Table 2, the efficiency of most algorithms is tightly correlated to the input hologram size, where Algorithm G is the fastest for the smaller input holograms (128 × 128 pixels), followed by the SM algorithm in the midrange input holograms (192 × 192 pixels) with Algorithm G closely after. Algorithm J then takes the lead for two of the larger input holograms tested, with Algorithms H, E, and F taking the lead for the rest. The MSE of the phase reconstruction relative to the true phase profile was found to be lowest when using the newly suggested Algorithm G, and is similar to the MSE yielded by Algorithms B and I.

An alternative rapid-processing approach based on off-axis holographic multiplexing that can reach up to 169 holograms of 512 × 512 pixels per second on a CPU have been introduced by Tahara *et al.* [228,229]. This method avoids using Fourier transforms in the hologram multiplexing. However, it utilizes smoothing in order to extract the desired sample wavefront from the spatially multiplexed hologram, with a trade-off between the filter size and the spatial bandwidth.

12. CONCLUSION AND PERSPECTIVES

We have presented the theory and applications of using multiplexing in off-axis digital holography, to enable single-shot acquisition of complex wavefronts, with more complex wavefront information compressed into the same camera plane, without an increase in the spatial bandwidth requirement of the camera. This special property of off-axis holography is derived from its usage of the redundancy in camera spatial bandwidth, namely that the off-axis fringes create a spatial frequency shift across a single axis, which leaves empty space across the other directions in the spatial frequency domain for additional terms to be compressed into the hologram. If the CC terms are not overlapping with any other term, they can be fully reconstructed, with a slight decrease in SNR due to the sharing of the camera gray-scale dynamic range in the hologram domain. The latter limitation is not significant for weakly scattering phase objects, such as cells *in vitro* and thin optical elements.

We have theoretically explained the multiplexing limit, which is six off-axis holograms for optical multiplexing, and methods to avoid unwanted cross terms between nonmatching beam pairs, which otherwise prevent full occupancy in the spatial frequency domain. We have also presented various experimental systems to implement off-axis holographic multiplexing, including interferometers built around the sample and external interferometric modules, which can be connected to existing

optical imaging systems. We have then reviewed various applications for off-axis holographic multiplexing, where each application requires a different optical system. These include FOV multiplexing, depth-of-field multiplexing, wavelength multiplexing, angular multiplexing, temporal event multiplexing, polarization multiplexing, and multimodal microscopy multiplexing of fluorescence and holography. Finally, we have shown that even if the multiplexing is not done digitally by projecting off-axis holograms of different fringe orientations on the camera, we can still perform the multiplexing of the off-axis holograms in the computer in order to gain rapid retrieval of the complex wavefronts encoded into the off-axis holograms, or to perform data compression, or more rapid optical visualization.

Of course, the main advantage of using off-axis holographic multiplexing is to speed up the acquisition of the complex wavefront data. Being able to perform highly rapid acquisition and processing of complex wavefronts in a quantitative, nondestructive, and nonintrusive manner is expected to open new horizons for biomedical and metrological applications. One specific future application that can benefit from holographic multiplexing is label-free holographic imaging flow cytometry [230–232]. In general, imaging flow cytometry is important for routine clinical analysis and diagnosis of diseases by providing high-throughput morphological analysis of thousands of cells per second in body fluids. Detecting and monitoring cancer, or other life-threatening conditions from body fluids, such as those obtained in routine lab tests, is a true clinical need, where flow cytometry is expected to allow access to many more cells than is possible in a conventional cell smear on a slide. Currently, imaging flow cytometry is capable of obtaining the morphological details of cells via fluorescence microscopy. In order to capture morphological images of the same cells, with numerous fluorescent labels per each cell, the realization of current imaging flow cytometers requires serially disposed laser towers, complicated spectral separation filters, and expensive cameras that image the same cell in multiple fluorescent imaging channels on different locations on the camera, demanding cameras with many pixels, complicated calibration routines, and extensive digital processing to avoid image registration problems. Cells *in vitro* are mostly transparent under regular light microscopy, and therefore cannot be measured well without using external stains or contrast agents, which is time consuming, might be harmful to the cells, and is not allowed in certain medical procedures. Since off-axis holography records the quantitative phase profile, which takes into account the cell refractive index and physical thickness, we can obtain the quantitative topographic maps of the cell from a single camera exposure, with great contrast and without the need for external contrast agents. Furthermore, even when using contrast agents in flow cytometry, the fact that phase profile is quantitative and accounts for the cell internal refractive indices gives rise to new parameters with medical relevance that were not available in flow cytometry before, such as the dry mass of the cells. To increase the analysis throughput and enable processing of large numbers of cells, flow cytometry uses extremely high flow rates. Specifically, in imaging flow cytometry, an imaging and processing rate of thousands of cells per second is needed, which is beyond the scope of the current holographic imaging techniques. Enabling optical hologram multiplexing is expected to allow the capturing and processing of the phase profiles of up to six times more cells, while increasing the quantitative cell imaging throughput and enabling the obtaining of real-time cell sorting decisions without using staining. If successful, this solution might dramatically change the field of imaging flow cytometry, being able to provide more cost-effective imaging flow cytometers with less expensive acquisition and processing units, and with improved quantitative analysis capabilities. Another closely related application that can benefit from off-axis holographic multiplexing is water inspection, for detecting microplastic particles and micro-organisms in water [233].

For nonbiological metrology, a possible future application is rapid profiling of metrological samples [30,234] to enable real-time feedback during rapid lithography or etching processes, which can enable improvement or alteration the process in real-time. An additional application is optical metrology of silicon wafers or other elements, which requires rapid scanning of extended sample areas and the profiling of the elements, in order to detect manufacturing defects. In this case, off-axis holographic multiplexing enables the acquisition of more information per sample instance, thus speeding up the scanning and enabling more rapid profiling.

Even if the process is not dynamic, holographic multiplexing can still help, since the noise characteristics might change between different camera exposures. Thus, if the complex wavefront information, which is typically acquired in several exposures taken at different time points, can now be compressed into a single multiplexed off-axis hologram, acquired in a single exposure, lower noise images can be obtained.

Indeed, hundreds of papers have been published on off-axis holographic multiplexing and its various applications over the years. The current paper provides the common theoretical basis and is expected to promote new research in this field, where the rapid measurements provided by off-axis holographic multiplexing can possibly enable new scientific findings and enable the complex wavefront measurement of rapid phenomena that could not be imaged until now.

Finally, please note that this review focuses on off-axis holographic multiplexing acquired in a single camera exposure for the general sample case, where it might not be sparse. However, the holographic multiplexing field is much wider, and it also includes different holographic geometries (e.g., on-axis). In addition, when the sample is sparse, the multiplexing can be done more efficiently based on the sample sparsity [235,236]. Furthermore, various mathematical tools of signal and image processing, such as wavelet compression [237–242], can be used for holographic multiplexing. Machine learning approaches in general and deep learning approaches in particular [19,243,244] can also be used for various types of holographic multiplexing directly, and for solving the inverse problem to retrieve data from the multiplexed holograms.

FUNDING

European Research Council (ERC StG 678316); Narodowe Centrum Nauki (2017/25/B/ST7/02049); Polish National Agency for Academic Exchange (PPN/BEK/2018/1/00511); Spanish Ministerio de Ciencia, Investigación y Universidades—Agencial Estatal de Investigación and the Fondo Europeo de Desarrollo Regional (FIS2017-89748-P); Foundation for Polish Science (TEAM TECH/2016-1/4).

DISCLOSURES

The authors declare no conflicts of interest.

REFERENCES

1. P. Marquet, B. Rappaz, P. J. Magistretti, E. Cuche, Y. Emery, T. Colomb, and C. Depeursinge, “Digital holographic microscopy: a noninvasive contrast imaging technique allowing quantitative visualization of living cells with subwavelength axial accuracy,” *Opt. Lett.* **30**, 468–470 (2005).
2. T. W. Su, L. Xue, and A. Ozcan, “High-throughput lensfree 3D tracking of human sperms reveals rare statistics of helical trajectories,” *Proc. Natl. Acad. Sci. USA* **109**, 16018–16022 (2012).

3. H. Gabai and N. T. Shaked, "Dual-channel low-coherence interferometry and its application to quantitative phase imaging of fingerprints," *Opt. Express* **20**, 26906–26912 (2012).
4. G. Coppola, P. Ferraro, M. Iodice, S. De Nicola, A. Finizio, and S. Grilli, "A digital holographic microscope for complete characterization of microelectromechanical systems," *Meas. Sci. Technol.* **15**, 529–539 (2004).
5. F. Merola, L. Miccio, P. Memmolo, G. Di Caprio, A. Galli, R. Puglisi, D. Balduzzi, G. Coppola, P. Netti, and P. Ferraro, "Digital holography as a method for 3D imaging and estimating the biovolume of motile cells," *Lab Chip* **13**, 4512–4516 (2013).
6. B. Rappaz, A. Barbul, Y. Emery, R. Korenstein, C. Depeursinge, P. J. Magistretti, and P. Marquet, "Comparative study of human erythrocytes by digital holographic microscopy, confocal microscopy, and impedance volume analyzer," *Cytometry Part A* **73A**, 895–903 (2008).
7. A. Nativ and N. T. Shaked, "Compact interferometric module for full-field interferometric phase microscopy with low spatial coherence illumination," *Opt. Lett.* **42**, 1492–1495 (2017).
8. R. Friedman and N. T. Shaked, "Hybrid reflective interferometric system combining wide-field and single-point phase measurements," *IEEE Photon. J.* **7**, 6801413 (2015).
9. H. Gabai, M. Baranes-Zeevi, M. Zilberman, and N. T. Shaked, "Continuous wide-field characterization of drug release from skin substitute using off-axis interferometry," *Opt. Lett.* **38**, 3017–3020 (2013).
10. P. Girshovitz and N. T. Shaked, "Compact and portable low-coherence interferometer with off-axis geometry for quantitative phase microscopy and nanoscopy," *Opt. Express* **21**, 5701–5714 (2013).
11. N. T. Shaked, "Quantitative phase microscopy of biological samples using a portable interferometer," *Opt. Lett.* **37**, 2016–2018 (2012).
12. A. W. Lohmann, "Reconstruction of vectorial wavefronts," *Appl. Opt.* **4**, 1667–1668 (1965).
13. I. Yamaguchi and T. Zhang, "Phase-shifting digital holography," *Opt. Lett.* **22**, 1268–1270 (1997).
14. J. E. Millerd, N. J. Brock, J. B. Hayes, M. B. North-Morris, M. Novak, and J. C. Wyant, "Pixelated phase-mask dynamic interferometer," *Proc. SPIE* **5531**, 304–314 (2004).
15. S. Murata and N. Yasuda, "Potential of digital holography in particle measurement," *Opt. Laser Technol.* **32**, 567–574 (2000).
16. W. Xu, M. H. Jericho, I. A. Meinertzhagen, and H. J. Kreuzer, "Digital in-line holography for biological applications," *Proc. Natl. Acad. Sci. USA* **98**, 11301–11305 (2001).
17. L. Martínez-León and B. Javidi, "Synthetic aperture single-exposure on-axis digital holography," *Opt. Express* **16**, 161–169 (2008).
18. H. Wang, M. Lyu, and G. Situ, "eHoloNet: a learning-based end-to-end approach for in-line digital holographic reconstruction," *Opt. Express* **26**, 22603–22614 (2018).
19. Y. Rivenson, Y. Wu, and A. Ozcan, "Deep learning in holography and coherent imaging," *Light Sci. Appl.* **8**, 85 (2019).
20. T. Kakue, R. Yonesaka, T. Tahara, Y. Awatsuji, K. Nishio, S. Ura, T. Kubota, and O. Matoba, "High-speed phase imaging by parallel phase-shifting digital holography," *Opt. Lett.* **36**, 4131–4133 (2011).
21. T. Tahara, R. Yonesaka, S. Yamamoto, T. Kakue, P. Xia, Y. Awatsuji, K. Nishio, S. Ura, T. Kubota, and O. Matoba, "High-speed three-dimensional microscope for dynamically moving biological objects based on parallel phase-shifting

- digital holographic microscopy,” *IEEE J. Sel. Top. Quantum Electron.* **18**, 1387–1393 (2012).
22. P. Xia, Y. Awatsuji, K. Nishio, and O. Matoba, “One million fps digital holography,” *Electron. Lett.* **50**, 1693–1695 (2014).
 23. T. Tahara, Y. Lee, Y. Ito, P. Xia, Y. Shimozato, Y. Takahashi, Y. Awatsuji, K. Nishio, S. Ura, T. Kubota, and O. Matoba, “Superresolution of interference fringes in parallel four-step phase-shifting digital holography,” *Opt. Lett.* **39**, 1673–1676 (2014).
 24. E. Sánchez-Ortiga, A. Doblas, G. Saavedra, M. Martínez-Corral, and J. Garcia-Sucerquia, “Off-axis digital holographic microscopy: practical design parameters for operating at diffraction limit,” *Appl. Opt.* **53**, 2058–2066 (2014).
 25. D. C. Ghiglia and M. D. Pritt, *Two-Dimensional Phase Unwrapping: Theory, Algorithms, and Software* (Wiley, 1998).
 26. I. Frenklach, P. Girshovitz, and N. T. Shaked, “Off-axis interferometric phase microscopy with tripled imaging area,” *Opt. Lett.* **39**, 1525–1528 (2014).
 27. J. Kühn, T. Colomb, F. Montfort, F. Charrière, Y. Emery, E. Cuche, P. Marquet, and C. Depeursinge, “Real-time dual-wavelength digital holographic microscopy with a single hologram acquisition,” *Opt. Express* **15**, 7231–7242 (2007).
 28. S. K. Mirsky and N. T. Shaked, “First experimental realization of six-pack holography and its application to dynamic synthetic aperture superresolution,” *Opt. Express* **27**, 26708–26720 (2019).
 29. Y. C. Lin, H. Y. Tu, X. R. Wu, X. J. Lai, and C. J. Cheng, “One-shot synthetic aperture digital holographic microscopy with non-coplanar angular-multiplexing and coherence gating,” *Opt. Express* **26**, 12620–12631 (2018).
 30. P. Girshovitz and N. T. Shaked, “Doubling the field of view in off-axis low-coherence interferometric imaging,” *Light Sci. Appl.* **3**, e151 (2014).
 31. D. Roitshtain, N. A. Turko, B. Javidi, and N. T. Shaked, “Flipping interferometry and its application for quantitative phase microscopy in a micro-channel,” *Opt. Lett.* **41**, 2354–2357 (2016).
 32. M. Rubin, G. Dardikman, S. K. Mirsky, N. A. Turko, and N. T. Shaked, “Six-pack off-axis holography,” *Opt. Lett.* **42**, 4611–4614 (2017).
 33. T. Tahara, Y. Awatsuji, K. Nishio, S. Ura, O. Matoba, and T. Kubota, “Space-bandwidth capacity-enhanced digital holography,” *Appl. Phys. Express* **6**, 22502 (2013).
 34. G. Dardikman and N. T. Shaked, “Is multiplexed off-axis holography for quantitative phase imaging more spatial bandwidth-efficient than on-axis holography?” *J. Opt. Soc. Am. A* **36**, A1–A11 (2019).
 35. B. Tayebi, Y. Jeong, and J. H. Han, “Dual-wavelength diffraction phase microscopy with 170 times larger image area,” *IEEE J. Sel. Top. Quantum Electron.* **25**, 7101206 (2018).
 36. B. Tayebi, J. H. Park, and J. Han, “Super-bandwidth two-step phase-shifting off-axis digital holography by optimizing two-dimensional spatial frequency sampling scheme,” *IEEE Access* **7**, 136836 (2019).
 37. G. Dardikman, N. A. Turko, N. Nativ, S. K. Mirsky, and N. T. Shaked, “Optimal spatial bandwidth capacity in multiplexed off-axis holography for rapid quantitative phase reconstruction and visualization,” *Opt. Express* **25**, 33400–33415 (2017).
 38. N. Pavillon, C. S. Seelamantula, J. Kühn, M. Unser, and C. Depeursinge, “Suppression of the zero-order term in off-axis digital holography through nonlinear filtering,” *Appl. Opt.* **48**, H186–H195 (2009).

39. C. S. Seelamantula, N. Pavillon, C. Depeursinge, and M. Unser, "Exact complex-wave reconstruction in digital holography," *J. Opt. Soc. Am. A* **28**, 983–992 (2011).
40. N. Pavillon, C. Arfire, I. Bergoënd, and C. Depeursinge, "Iterative method for zero-order suppression in off-axis digital holography," *Opt. Express* **18**, 15318–15331 (2010).
41. D. Zhao, D. Xie, Y. Yang, and H. Zhai, "Iterative approach for zero-order term elimination in off-axis multiplex digital holography," *Opt. Commun.* **383**, 513–517 (2017).
42. Y. Baek, K. Lee, S. Shin, and Y. Park, "Kramers–Kronig holographic imaging for high-space-bandwidth product," *Optica* **6**, 45–51 (2019).
43. N. T. Shaked, Y. Zhu, M. T. Rinehart, and A. Wax, "Two-step-only phase-shifting interferometry with optimized detector bandwidth for microscopy of live cells," *Opt. Express* **17**, 15585–15591 (2009).
44. L. Xue, J. Lai, S. Wang, and Z. Li, "Single-shot slightly-off-axis interferometry based Hilbert phase microscopy of red blood cells," *Biomed. Opt. Express* **2**, 987–995 (2011).
45. T. Ikeda, G. Popescu, R. R. Dasari, and M. S. Feld, "Hilbert phase microscopy for investigating fast dynamics in transparent systems," *Opt. Lett.* **30**, 1165–1167 (2005).
46. M. Trusiak, J. Picazo-Bueno, K. Patorski, P. Zdankowski, and V. Mico, "Single-shot two-frame π -shifted spatially multiplexed interference phase microscopy," *J. Biomed. Opt.* **24**, 1–8 (2019).
47. J. A. Picazo-Bueno, M. Trusiak, and V. Micó, "Single-shot slightly off-axis digital holographic microscopy with add-on module based on beamsplitter cube," *Opt. Express* **27**, 5655–5669 (2019).
48. J. Min, B. Yao, P. Gao, R. Guo, B. Ma, J. Zheng, M. Lei, S. Yan, D. Dan, T. Duan, Y. Yang, and T. Ye, "Dual-wavelength slightly off-axis digital holographic microscopy," *Appl. Opt.* **51**, 191–196 (2012).
49. Z. Zhong, H. Bai, M. Shan, Y. Zhang, and L. Guo, "Fast phase retrieval in slightly off-axis digital holography," *Opt. Laser Eng.* **97**, 9–18 (2017).
50. O. Matoba, T. J. Naughton, Y. Frauel, N. Bertaux, and B. Javidi, "Real-time three-dimensional object reconstruction by use of a phase-encoded digital hologram," *Appl. Opt.* **41**, 6187–6192 (2002).
51. I. Yamaguchi, K. Yamamoto, G. A. Mills, and M. Yokota, "Image reconstruction only by phase data in phase-shifting digital holography," *Appl. Opt.* **45**, 975–983 (2006).
52. P. Girshovitz, I. Frenklach, and N. T. Shaked, "Broadband quantitative phase microscopy with extended field of view using off-axis interferometric multiplexing," *J. Biomed. Opt.* **20**, 111217 (2015).
53. N. Rotman-Nativ, N. A. Turko, and N. T. Shaked, "Flipping interferometry with doubled imaging area," *Opt. Lett.* **43**, 5543–5546 (2018).
54. V. Chhaniwal, A. S. G. Singh, R. A. Leitgeb, B. Javidi, and A. Anand, "Quantitative phase-contrast imaging with compact digital holographic microscope employing Lloyd's mirror," *Opt. Lett.* **37**, 5127–5129 (2012).
55. V. Mico, C. Ferreira, Z. Zalevsky, and J. García, "Spatially-multiplexed interferometric microscopy (SMIM): converting a standard microscope into a holographic one," *Opt. Express* **22**, 14929–14943 (2014).
56. A. S. G. Singh, A. Anand, R. A. Leitgeb, and B. Javidi, "Lateral shearing digital holographic imaging of small biological specimens," *Opt. Express* **20**, 23617–23622 (2012).

57. K. Seo, B. M. Kim, and E. S. Kim, "Digital holographic microscopy based on a modified lateral shearing interferometer for three-dimensional visual inspection of nanoscale defects on transparent objects," *Nanoscale Res. Lett.* **9**, 471 (2014).
58. B. M. Kim and E. S. Kim, "Visual inspection of 3-D surface and refractive-index profiles of microscopic lenses using a single-arm off-axis holographic interferometer," *Opt. Express* **24**, 10326–10344 (2016).
59. L. Han, Z. J. Cheng, Y. Yang, B. Y. Wang, Q. Y. Yue, and C. S. Guo, "Double-channel angular-multiplexing polarization holography with common-path and off-axis configuration," *Opt. Express* **25**, 21877–21886 (2017).
60. T. Sun, P. Lu, Z. Zhuo, W. Zhang, and J. Lu, "Single-shot two-channel Fresnel bimirror interferometric microscopy for quantitative phase imaging of biological cell," *Opt. Commun.* **426**, 77–83 (2018).
61. S. Ebrahimi, M. Dashtdar, E. Sánchez-Ortiga, M. Martínez-Corral, and B. Javidi, "Stable and simple quantitative phase-contrast imaging by Fresnel biprism," *Appl. Phys. Lett.* **112**, 113701 (2018).
62. T. Sun, Z. Zhuo, W. Zhang, J. Lu, and P. Lu, "Single-shot interference microscopy using a wedged glass plate for quantitative phase imaging of biological cells," *Laser Phys.* **28**, 125601 (2018).
63. S. Yokozeki and T. Suzuki, "Shearing interferometer using the grating as the beam splitter," *Appl. Opt.* **10**, 1575–1580 (1971).
64. A. W. Lohmann and D. E. Silva, "An interferometer based on the Talbot effect," *Opt. Commun.* **2**, 413–415 (1971).
65. K. Patorski, "The self-imaging phenomenon and its applications," in *Progress in Optics*, E. Wolf, ed. (North-Holland, 1989), Vol. **27**, pp. 1–108.
66. J. A. Quiroga, D. Crespo, and E. Bernabeu, "Fourier transform method for automatic processing of moire deflectograms," *Opt. Eng.* **38**, 974–982 (1999).
67. K. Patorski, M. Trusiak, and K. Pokorski, "Single-shot two-channel Talbot interferometry using checker grating and Hilbert-Huang fringe pattern processing," *Proc. SPIE* **9132**, 91320Z (2014).
68. J. Primot and N. Guérineau, "Extended Hartmann test based on the pseudoguiding property of a Hartmann mask completed by a phase chessboard," *Appl. Opt.* **39**, 5715–5720 (2000).
69. K. Patorski, Ł. Służewski, P. Zdańkowski, M. Cywińska, and M. Trusiak, "Three-level transmittance 2D grating with reduced spectrum and its self-imaging," *Opt. Express* **27**, 1854–1868 (2019).
70. T. Ling, D. Liu, X. Yue, Y. Yang, Y. Shen, and J. Bai, "Quadriwave lateral shearing interferometer based on a randomly encoded hybrid grating," *Opt. Lett.* **40**, 2245–2248 (2015).
71. R. Legarda-Sáenz and A. Espinosa-Romero, "Wavefront reconstruction using multiple directional derivatives and Fourier transform," *Opt. Eng.* **50**, 040501 (2011).
72. S. Velghe, J. Primot, N. Guérineau, M. Cohen, and B. Wattellier, "Wave-front reconstruction from multidirectional phase derivatives generated by multilateral shearing interferometers," *Opt. Lett.* **30**, 245–247 (2005).
73. S. Velghe, J. Primot, N. Guérineau, R. Haidar, M. Cohen, and B. Wattellier, "Accurate and highly resolving quadri-wave lateral shearing interferometer, from visible to IR," *Proc. SPIE* **5776**, 134–143 (2005).
74. P. Bon, G. Maucort, B. Wattellier, and S. Monneret, "Quadriwave lateral shearing interferometry for quantitative phase microscopy of living cells," *Opt. Express* **17**, 13080–13094 (2009).
75. S. Aknoun, P. Bon, J. Savatier, B. Wattellier, and S. Monneret, "Quantitative retardance imaging of biological samples using quadriwave lateral shearing interferometry," *Opt. Express* **23**, 16383–16406 (2015).

76. K. Patorski, Ł. Służewski, and M. Trusiak, "Single-shot 3×3 beam grating interferometry for self-imaging free extended range wave front sensing," *Opt. Lett.* **41**, 4417–4420 (2016).
77. K. Patorski, Ł. Służewski, and M. Trusiak, "5-beam grating interferometry for extended phase gradient sensing," *Opt. Express* **26**, 26872–26887 (2018).
78. P. Langehanenberg, L. Ivanova, I. Bernhardt, S. Ketelhut, A. Vollmer, D. Dirksen, G. K. Georgiev, G. von Bally, and B. Kemper, "Automated three-dimensional tracking of living cells by digital holographic microscopy," *J. Biomed. Opt.* **14**, 014018 (2009).
79. P. M. Blanchard and A. H. Greenaway, "Simultaneous multiplane imaging with a distorted diffraction grating," *Appl. Opt.* **38**, 6692–6699 (1999).
80. P. A. Dalgarno, H. I. C. Dalgarno, A. Putoud, R. Lambert, L. Paterson, D. C. Logan, D. P. Towers, R. J. Warburton, and A. H. Greenaway, "Multiplane imaging and three dimensional nanoscale particle tracking in biological microscopy," *Opt. Express* **18**, 877–884 (2010).
81. M. McGuire, W. Matusik, H. Pfister, B. Chen, J. F. Hughes, and S. K. Nayar, "Optical splitting trees for high-precision monocular imaging," *IEEE Comput. Graph. Applic.* **27**, 32–42 (2007).
82. C. Maurer, S. Khan, S. Fassel, S. Bernet, and M. Ritsch-Marte, "Depth of field multiplexing in microscopy," *Opt. Express* **18**, 3023–3034 (2010).
83. P. Ferraro, M. Paturzo, P. Memmolo, and A. Finizio, "Controlling depth of focus in 3D image reconstructions by flexible and adaptive deformation of digital holograms," *Opt. Lett.* **34**, 2787–2789 (2009).
84. J. Kostencka, T. Kozacki, and K. Liżewski, "Autofocusing method for tilted image plane detection in digital holographic microscopy," *Opt. Commun.* **297**, 20–26 (2013).
85. M. Paturzo, A. Finizio, and P. Ferraro, "Simultaneous multiplane imaging in digital holographic microscopy," *J. Disp. Technol.* **7**, 24–28 (2011).
86. W. Pan, "Multiplane imaging and depth-of-focus extending in digital holography by a single-shot digital hologram," *Opt. Commun.* **286**, 117–122 (2013).
87. M. Matrecano, M. Paturzo, and P. Ferraro, "Extended focus imaging in digital holographic microscopy: a review," *Opt. Eng.* **53**, 112317 (2014).
88. L. Wolbromsky, N. A. Turko, and N. T. Shaked, "Single-exposure full-field multi-depth imaging using low-coherence holographic multiplexing," *Opt. Lett.* **43**, 2046–2049 (2018).
89. S. Schedin, G. Pedrini, H. J. Tiziani, and F. M. Santoyo, "Simultaneous three-dimensional dynamic deformation measurements with pulsed digital holography," *Appl. Opt.* **38**, 7056–7062 (1999).
90. P. Picart, E. Moisson, and D. Mounier, "Twin-sensitivity measurement by spatial multiplexing of digitally recorded holograms," *Appl. Opt.* **42**, 1947–1957 (2003).
91. T. Saucedo-A, M. H. De la Torre-Ibarra, F. M. Santoyo, and I. Moreno, "Digital holographic interferometer using simultaneously three lasers and a single monochrome sensor for 3D displacement measurements," *Opt. Express* **18**, 19867–19875 (2010).
92. P. Tankam, Q. Song, M. Karray, J. Li, J. M. Dese, and P. Picart, "Real-time three-sensitivity measurements based on three-color digital Fresnel holographic interferometry," *Opt. Lett.* **35**, 2055–2057 (2010).
93. A. T. Saucedo, F. M. Santoyo, M. H. De la Torre-Ibarra, G. Pedrini, and W. Osten, "Endoscopic pulsed digital holography for 3D measurements," *Opt. Express* **14**, 1468–1475 (2006).

94. B. Tayebi, M. R. Jafarfard, F. Sharif, Y. S. Bae, S. H. H. Shokuh, and D. Y. Kim, "Reduced-phase dual-illumination interferometer for measuring large stepped objects," *Opt. Lett.* **39**, 5740–5743 (2014).
95. B. Tayebi, M. R. Jafarfard, F. Sharif, Y. S. Song, D. Har, and D. Y. Kim, "Large step-phase measurement by a reduced-phase triple-illumination interferometer," *Opt. Express* **23**, 11264–11271 (2015).
96. P. Memmolo, A. Finizio, M. Paturzo, L. Miccio, and P. Ferraro, "Twin-beams digital holography for 3D tracking and quantitative phase-contrast microscopy in microfluidics," *Opt. Express* **19**, 25833–25842 (2011).
97. P. Memmolo, L. Miccio, M. Paturzo, G. Di Caprio, G. Coppola, P. A. Netti, and P. Ferraro, "Recent advances in holographic 3D particle tracking," *Adv. Opt. Photon.* **7**, 713–755 (2015).
98. S. M. Azzem, L. Bouamama, S. Simoëns, and W. Osten, "Two beams two orthogonal views particle detection," *J. Opt.* **17**, 45301 (2015).
99. Z. Ren, Z. Xu, and E. Y. Lam, "Learning-based nonparametric autofocusing for digital holography," *Optica* **5**, 337–344 (2018).
100. Y. Wu, Y. Rivenson, Y. Zhang, Z. Wei, H. Günaydin, X. Lin, and A. Ozcan, "Extended depth-of-field in holographic imaging using deep-learning-based autofocusing and phase recovery," *Optica* **5**, 704–710 (2018).
101. H. Pinkard, Z. Phillips, A. Babakhani, D. A. Fletcher, and L. Waller, "Deep learning for single-shot autofocus microscopy," *Optica* **6**, 794–797 (2019).
102. C. Polhemus, "Two-wavelength interferometry," *Appl. Opt.* **12**, 2071–2074 (1973).
103. J. Gass, A. Dakoff, and M. K. Kim, "Phase imaging without 2π ambiguity by multiwavelength digital holography," *Opt. Lett.* **28**, 1141–1143 (2003).
104. M. T. Rinehart, N. T. Shaked, N. J. Jenness, R. L. Clark, and A. Wax, "Simultaneous two-wavelength transmission quantitative phase microscopy with a color camera," *Opt. Lett.* **35**, 2612–2614 (2010).
105. D. G. Abdelsalam and D. Kim, "Real-time dual-wavelength digital holographic microscopy based on polarizing separation," *Opt. Commun.* **285**, 233–237 (2012).
106. A. Khmaladze, A. Restrepo-Martínez, M. Kim, R. Castañeda, and A. Blandón, "Simultaneous dual-wavelength reflection digital holography applied to the study of the porous coal samples," *Appl. Opt.* **47**, 3203–3210 (2008).
107. A. Khmaladze, M. Kim, and C. M. Lo, "Phase imaging of cells by simultaneous dual-wavelength reflection digital holography," *Opt. Express* **16**, 10900–10911 (2008).
108. B. Kemper, F. Schlichthaber, A. Vollmer, S. Ketelhut, S. Przibilla, and G. von Bally, "Self interference digital holographic microscopy approach for inspection of technical and biological phase specimens," *Proc. SPIE* **8082**, 808207 (2011).
109. B. Bhaduri, H. Pham, M. Mir, and G. Popescu, "Diffraction phase microscopy with white light," *Opt. Lett.* **37**, 1094–1096 (2012).
110. N. A. Turko and N. T. Shaked, "Simultaneous two-wavelength phase unwrapping using an external module for multiplexing off-axis holography," *Opt. Lett.* **42**, 73–76 (2017).
111. F. Montfort, T. Colomb, F. Charrière, J. Kühn, P. Marquet, E. Cuche, S. Herminjard, and C. Depeursinge, "Submicrometer optical tomography by multiple-wavelength digital holographic microscopy," *Appl. Opt.* **45**, 8209–8217 (2006).
112. C. J. Mann, P. R. Bingham, V. C. Paquit, and K. W. Tobin, "Quantitative phase imaging by three-wavelength digital holography," *Opt. Express* **16**, 9753–9764 (2008).

113. Y. Li, W. Xiao, and F. Pan, "Multiple-wavelength-scanning-based phase unwrapping method for digital holographic microscopy," *Appl. Opt.* **53**, 979–987 (2014).
114. J. M. Desse and P. Picart, "Quasi-common path three-wavelength holographic interferometer based on Wollaston prisms," *Opt. Laser Eng.* **68**, 188–193 (2015).
115. N. A. Turko, P. J. Eravuchira, I. Barnea, and N. T. Shaked, "Simultaneous three-wavelength unwrapping using external digital holographic multiplexing module," *Opt. Lett.* **43**, 1943–1946 (2018).
116. Y. Jang, J. Jang, and Y. Park, "Dynamic spectroscopic phase microscopy for quantifying hemoglobin concentration and dynamic membrane fluctuation in red blood cells," *Opt. Express* **20**, 9673–9681 (2012).
117. N. Lue, J. W. Kang, T. R. Hillman, R. R. Dasari, and Z. Yaqoob, "Single-shot quantitative dispersion phase microscopy," *Appl. Phys. Lett.* **101**, 84101 (2012).
118. T. Tahara, T. Kaku, and Y. Arai, "Digital holography based on multiwavelength spatial-bandwidth-extended capturing-technique using a reference arm (Multi-SPECTRA)," *Opt. Express* **22**, 29594–29610 (2014).
119. B. Tayebi, W. Kim, F. Sharif, B. Yoon, and J. Han, "Single-shot and label-free refractive index dispersion of single nerve fiber by triple-wavelength diffraction phase microscopy," *IEEE J. Sel. Top. Quantum Electron.* **25**, 7200708 (2019).
120. M. R. Jafarfard, S. Moon, B. Tayebi, and D. Y. Kim, "Dual-wavelength diffraction phase microscopy for simultaneous measurement of refractive index and thickness," *Opt. Lett.* **39**, 2908–2911 (2014).
121. E. Abbe, "Beiträge zur Theorie des Mikroskops und der mikroskopischen Wahrnehmung: IV. Das optische Vermögen des Mikroskops," *Arch. für mikroskopische Anat.* **9**, 413–468 (1873).
122. E. Helmholtz and H. Fripp, "On the limits of the optical capacity of the microscope," *Mon. Microsc. J.* **16**, 15–39 (1876).
123. L. Rayleigh, "XV. On the theory of optical images, with special reference to the microscope," *London, Edinburgh, Dublin Philos. Mag. J. Sci.* **42**, 167–195 (1896).
124. A. B. Porter, "XII. On the diffraction theory of microscopic vision," *London, Edinburgh, Dublin Philos. Mag. J. Sci.* **11**, 154–166 (1906).
125. M. Born, E. Wolf, A. B. Bhatia, P. C. Clemmow, D. Gabor, A. R. Stokes, A. M. Taylor, P. A. Wayman, and W. L. Wilcock, *Principles of Optics: Electromagnetic Theory of Propagation, Interference and Diffraction of Light*, 7th ed. (Cambridge University, 1999).
126. Y. Cotte, M. F. Toy, E. Shaffer, N. Pavillon, and C. Depeursinge, "Sub-Rayleigh resolution by phase imaging," *Opt. Lett.* **35**, 2176–2178 (2010).
127. R. Horstmeyer, R. Heintzmann, G. Popescu, L. Waller, and C. Yang, "Standardizing the resolution claims for coherent microscopy," *Nat. Photonics* **10**, 68–71 (2016).
128. M. K. Kim, "Principles and techniques of digital holographic microscopy," *SPIE Rev.* **1**, 1–51 (2010).
129. M. K. Kim, *Digital Holographic Microscopy: Principles, Techniques, and Applications* (Springer, 2011).
130. N. T. Shaked, Z. Zalevsky, and L. L. Satterwhite, *Biomedical Optical Phase Microscopy and Nanoscopy* (Academic, 2012).
131. J. J. Cargille, *Immersion Oil and the Microscope* (New York Microscopical Society Yearbook, 1964).
132. V. Micó, Z. Zalevsky, and J. Garcia-Monreal, "Optical superresolution: imaging beyond Abbe's diffraction limit," *J. Hologr. Speckle* **5**, 110–123 (2009).

133. V. Micó, J. Zheng, J. Garcia, Z. Zalevsky, and P. Gao, "Resolution enhancement in quantitative phase microscopy," *Adv. Opt. Photon.* **11**, 135–214 (2019).
134. M. Ueda and T. Sato, "Superresolution by holography," *J. Opt. Soc. Am.* **61**, 418–419 (1971).
135. M. Ueda, T. Sato, and M. Kondo, "Superresolution by multiple superposition of image holograms having different carrier frequencies," *Opt. Acta Int. J. Opt.* **20**, 403–410 (1973).
136. T. Sato, M. Ueda, and G. Yamagishi, "Superresolution microscope using electrical superposition of holograms," *Appl. Opt.* **13**, 406–408 (1974).
137. T. Sato, M. Ueda, and T. Ikeda, "Real time superresolution by means of an ultrasonic light diffractor and TV system," *Appl. Opt.* **13**, 1318–1321 (1974).
138. W. T. Cathey, B. R. Frieden, W. T. Rhodes, and C. K. Rushforth, "Image gathering and processing for enhanced resolution," *J. Opt. Soc. Am. A* **1**, 241–250 (1984).
139. A. J. den Dekker and A. van den Bos, "Resolution: a survey," *J. Opt. Soc. Am. A* **14**, 547–557 (1997).
140. Z. Zalevsky and D. Mendlovic, *Optical Superresolution* (Springer, 2004).
141. Z. Zalevsky, V. Micó, and J. Garcia, "Nanophotonics for optical super resolution from an information theoretical perspective: a review," *J. Nanophoton.* **3**, 032502 (2009).
142. E. N. Leith, D. Angell, and C. P. Kuei, "Superresolution by incoherent-to-coherent conversion," *J. Opt. Soc. Am. A* **4**, 1050–1054 (1987).
143. E. N. Leith, "Small-aperture, high-resolution, two-channel imaging system," *Opt. Lett.* **15**, 885–887 (1990).
144. W. Lukosz, "Optical systems with resolving powers exceeding the classical limit," *J. Opt. Soc. Am.* **56**, 1463–1471 (1966).
145. W. Lukosz, "Optical systems with resolving powers exceeding the classical limit. II," *J. Opt. Soc. Am.* **57**, 932–941 (1967).
146. P. C. Sun and E. N. Leith, "Superresolution by spatial-temporal encoding methods," *Appl. Opt.* **31**, 4857–4862 (1992).
147. V. Mico, Z. Zalevsky, P. Garcia-Martinez, and J. Garcia, "Single-step superresolution by interferometric imaging," *Opt. Express* **12**, 2589–2596 (2004).
148. V. Mico, Z. Zalevsky, P. García-Martínez, and J. García, "Superresolved imaging in digital holography by superposition of tilted wavefronts," *Appl. Opt.* **45**, 822–828 (2006).
149. V. Mico, Z. Zalevsky, P. García-Martínez, and J. García, "Synthetic aperture superresolution with multiple off-axis holograms," *J. Opt. Soc. Am. A* **23**, 3162–3170 (2006).
150. L. Granero, Z. Zalevsky, and V. Micó, "Single-exposure two-dimensional superresolution in digital holography using a vertical cavity surface-emitting laser source array," *Opt. Lett.* **36**, 1149–1151 (2011).
151. C. Liu, Z. Liu, F. Bo, Y. Wang, and J. Zhu, "Super-resolution digital holographic imaging method," *Appl. Phys. Lett.* **81**, 3143–3145 (2002).
152. M. Paturzo, F. Merola, S. Grilli, S. De Nicola, A. Finizio, and P. Ferraro, "Superresolution in digital holography by a two-dimensional dynamic phase grating," *Opt. Express* **16**, 17107–17118 (2008).
153. M. Paturzo and P. Ferraro, "Correct self-assembling of spatial frequencies in super-resolution synthetic aperture digital holography," *Opt. Lett.* **34**, 3650–3652 (2009).
154. L. Granero, V. Micó, Z. Zalevsky, and J. García, "Superresolution imaging method using phase-shifting digital lensless Fourier holography," *Opt. Express* **17**, 15008–15022 (2009).

155. C. Yuan, H. Zhai, and H. Liu, "Angular multiplexing in pulsed digital holography for aperture synthesis," *Opt. Lett.* **33**, 2356–2358 (2008).
156. J. Zhao, X. Yan, W. Sun, and J. Di, "Resolution improvement of digital holographic images based on angular multiplexing with incoherent beams in orthogonal polarization states," *Opt. Lett.* **35**, 3519–3521 (2010).
157. C. Yuan, G. Situ, G. Pedrini, J. Ma, and W. Osten, "Resolution improvement in digital holography by angular and polarization multiplexing," *Appl. Opt.* **50**, B6–B11 (2011).
158. H. Y. Tu, X. J. Lai, Y. C. Lin, and C. J. Cheng, "Angular- and polarization-multiplexing with spatial light modulators for resolution enhancement in digital holographic microscopy," in *Digital Holography & 3-D Imaging Meeting* (Optical Society of America, 2015), paper DT3A.4.
159. S. Li, J. Ma, C. Chang, S. Nie, S. Feng, and C. Yuan, "Phase-shifting-free resolution enhancement in digital holographic microscopy under structured illumination," *Opt. Express* **26**, 23572–23584 (2018).
160. A. Calabuig, V. Micó, J. Garcia, Z. Zalevsky, and C. Ferreira, "Single-exposure super-resolved interferometric microscopy by red–green–blue multiplexing," *Opt. Lett.* **36**, 885–887 (2011).
161. A. Calabuig, J. Garcia, C. Ferreira, Z. Zalevsky, and V. Micó, "Resolution improvement by single-exposure superresolved interferometric microscopy with a monochrome sensor," *J. Opt. Soc. Am. A* **28**, 2346–2358 (2011).
162. L. Granero, C. Ferreira, Z. Zalevsky, J. García, and V. Micó, "Single-exposure super-resolved interferometric microscopy by RGB multiplexing in lensless configuration," *Opt. Laser Eng.* **82**, 104–112 (2016).
163. M. Kim, Y. Choi, C. Fang-Yen, Y. Sung, R. R. Dasari, M. S. Feld, and W. Choi, "High-speed synthetic aperture microscopy for live cell imaging," *Opt. Lett.* **36**, 148–150 (2011).
164. Y. Sung, W. Choi, N. Lue, R. R. Dasari, and Z. Yaqoob, "Stain-free quantification of chromosomes in live cells using regularized tomographic phase microscopy," *PLoS One* **7**, 1–7 (2012).
165. W. Choi, C. Fang-Yen, K. Badizadegan, S. Oh, N. Lue, R. R. Dasari, and M. S. Feld, "Tomographic phase microscopy," *Nat. Methods* **4**, 717–719 (2007).
166. M. Kim, Y. Choi, W. Choi, C. M. Fang-Yen, Y. Sung, R. R. Dasari, M. S. Feld, and K. Kim, "Three-dimensional differential interference contrast microscopy using synthetic aperture imaging," *J. Biomed. Opt.* **17**, 026003 (2012).
167. Y. Sung, A. Tzur, S. Oh, W. Choi, V. Li, R. R. Dasari, Z. Yaqoob, and M. W. Kirschner, "Size homeostasis in adherent cells studied by synthetic phase microscopy," *Proc. Natl. Acad. Sci. USA* **110**, 16687–16692 (2013).
168. K. Kim, K. S. Kim, H. Park, J. C. Ye, and Y. Park, "Real-time visualization of 3-D dynamic microscopic objects using optical diffraction tomography," *Opt. Express* **21**, 32269–32278 (2013).
169. B. Simon, M. Debailleul, M. Houkal, C. Ecoffet, J. Bailleul, J. Lambert, A. Spangenberg, H. Liu, O. Soppera, and O. Haeberlé, "Tomographic diffractive microscopy with isotropic resolution," *Optica* **4**, 460–463 (2017).
170. J. Bailleul, B. Simon, M. Debailleul, L. Foucault, N. Verrier, and O. Haeberlé, "Tomographic diffractive microscopy: towards high-resolution 3-D real-time data acquisition, image reconstruction and display of unlabeled samples," *Opt. Commun.* **422**, 28–37 (2018).
171. L. Foucault, N. Verrier, M. Debailleul, B. Simon, and O. Haeberlé, "Simplified tomographic diffractive microscopy for axisymmetric samples," *OSA Continuum* **2**, 1039–1055 (2019).
172. Y. Park, C. Depeursinge, and G. Popescu, "Quantitative phase imaging in biomedicine," *Nat. Photonics* **12**, 578–589 (2018).

173. E. Wolf, "Three-dimensional structure determination of semi-transparent objects from holographic data," *Opt. Commun.* **1**, 153–156 (1969).
174. A. Kuś, W. Krauze, P. L. Makowski, and M. Kujawińska, "Holographic tomography: hardware and software solutions for 3D quantitative biomedical imaging," *ETRI J.* **41**, 61–72 (2019).
175. C. J. R. Sheppard and S. S. Kou, "3D imaging with holographic tomography," *AIP Conf. Proc.* **1236**, 65–69 (2010).
176. F. Charrière, A. Marian, F. Montfort, J. Kuehn, T. Colomb, E. Cuche, P. Marquet, and C. Depeursinge, "Cell refractive index tomography by digital holographic microscopy," *Opt. Lett.* **31**, 178–180 (2006).
177. A. Kuś, M. Dudek, B. Kemper, M. Kujawińska, and A. Vollmer, "Tomographic phase microscopy of living three-dimensional cell cultures," *J. Biomed. Opt.* **19**, 046009 (2014).
178. C. M. Fang-Yen, W. Choi, Y. Sung, C. J. Holbrow, R. R. Dasari, and M. S. Feld, "Video-rate tomographic phase microscopy," *J. Biomed. Opt.* **16**, 011005 (2011).
179. D. Jin, R. Zhou, Z. Yaqoob, and P. T. C. So, "Dynamic spatial filtering using a digital micromirror device for high-speed optical diffraction tomography," *Opt. Express* **26**, 428–437 (2018).
180. K. Kim, J. Yoon, and Y. Park, "Simultaneous 3D visualization and position tracking of optically trapped particles using optical diffraction tomography," *Optica* **2**, 343–346 (2015).
181. W. Krauze, P. Makowski, M. Kujawińska, and A. Kuś, "Generalized total variation iterative constraint strategy in limited angle optical diffraction tomography," *Opt. Express* **24**, 4924–4936 (2016).
182. K. Franke, "Tomographic apparatus for producing transverse layer images," U.S. patent 4,150,293 (17 April 1979).
183. E. L. Ritman, J. H. Kinsey, R. A. Robb, B. K. Gilbert, L. D. Harris, and E. H. Wood, "Three-dimensional imaging of heart, lungs, and circulation," *Science* **210**, 273–280 (1980).
184. E. Niemi, M. Lassas, and S. Siltanen, "Dynamic x-ray tomography with multiple sources," in *8th International Symposium on Image and Signal Processing and Analysis (ISPA)* (2013), pp. 618–621.
185. L. Chen, N. Andrews, S. Kumar, P. Frankel, J. McGinty, and P. M. W. French, "Simultaneous angular multiplexing optical projection tomography at shifted focal planes," *Opt. Lett.* **38**, 851–853 (2013).
186. G. Barbastathis and D. Psaltis, "Volume holographic multiplexing methods," in *Holographic Data Storage*, H. J. Coufal, D. Psaltis, and G. T. Sincerbox, eds. (Springer, 2000), pp. 21–62.
187. E. N. Leith, A. Kozma, J. Upatnieks, J. Marks, and N. Massey, "Holographic data storage in three-dimensional media," *Appl. Opt.* **5**, 1303–1311 (1966).
188. M. Kujawinska, A. Jozwicka, and T. Kozacki, "Investigations and improvements of digital holographic tomography applied for 3D studies of transmissive photonics microelements," *Proc. SPIE* **7063**, 70630F (2008).
189. E. Mudry, P. C. Chaumet, K. Belkebir, G. Maire, and A. Sentenac, "Mirror-assisted tomographic diffractive microscopy with isotropic resolution," *Opt. Lett.* **35**, 1857–1859 (2010).
190. J. Kostencka, T. Kozacki, and M. Józwick, "Holographic tomography with object rotation and two-directional off-axis illumination," *Opt. Express* **25**, 23920–23934 (2017).
191. P. Hosseini, Y. Sung, Y. Choi, N. Lue, Z. Yaqoob, and P. So, "Scanning color optical tomography (SCOT)," *Opt. Express* **23**, 19752–19762 (2015).

192. S. Chowdhury, W. J. Eldridge, A. Wax, and J. Izatt, "Refractive index tomography with structured illumination," *Optica* **4**, 537–545 (2017).
193. V. Balasubramani, H. Y. Tu, X. J. Lai, and C. J. Cheng, "Adaptive wavefront correction structured illumination holographic tomography," *Sci. Rep.* **9**, 10489 (2019).
194. K. Lee, K. Kim, G. Kim, S. Shin, and Y. Park, "Time-multiplexed structured illumination using a DMD for optical diffraction tomography," *Opt. Lett.* **42**, 999–1002 (2017).
195. Y. Sung, "Snapshot holographic optical tomography," *Phys. Rev. Appl.* **11**, 14039 (2019).
196. A. Kuś, W. Krauze, and M. Kujawińska, "Active limited-angle tomographic phase microscope," *J. Biomed. Opt.* **20**, 111216 (2015).
197. Y. He, Y. Wang, and R. Zhou, "Digital micromirror device based angle-multiplexed optical diffraction tomography for high throughput 3D imaging of cells," *Proc. SPIE* **11294**, 1129402 (2020).
198. A. Kuś, M. Baczewska, M. Ziemczonok, and M. Kujawińska, "Projection multiplexing for enhanced acquisition speed in holographic tomography," *Proc. SPIE* **10883**, 1088318 (2019).
199. G. Dardikman, G. Singh, and N. T. Shaked, "Four dimensional phase unwrapping of dynamic objects in digital holography," *Opt. Express* **26**, 3772–3778 (2018).
200. Y. Park, G. Popescu, K. Badizadegan, R. R. Dasari, and M. S. Feld, "Diffraction phase and fluorescence microscopy," *Opt. Express* **14**, 8263–8268 (2006).
201. E. Shaffer, N. Pavillon, and C. Depeursinge, "Single-shot, simultaneous incoherent and holographic microscopy," *J. Microsc.* **245**, 49–62 (2012).
202. S. Chowdhury, W. J. Eldridge, A. Wax, and J. A. Izatt, "Spatial frequency-domain multiplexed microscopy for simultaneous, single-camera, one-shot, fluorescent, and quantitative-phase imaging," *Opt. Lett.* **40**, 4839–4842 (2015).
203. Y. N. Nygate, G. Singh, I. Barnea, and N. T. Shaked, "Simultaneous off-axis multiplexed holography and regular fluorescence microscopy of biological cells," *Opt. Lett.* **43**, 2587–2590 (2018).
204. Z. Liu, M. Centurion, G. Panotopoulos, J. Hong, and D. Psaltis, "Holographic recording of fast events on a CCD camera," *Opt. Lett.* **27**, 22–24 (2002).
205. X. Wang, H. Zhai, and G. Mu, "Pulsed digital holography system recording ultrafast process of the femtosecond order," *Opt. Lett.* **31**, 1636–1638 (2006).
206. X. Wang and H. Zhai, "Pulsed digital micro-holography of femto-second order by wavelength division multiplexing," *Opt. Commun.* **275**, 42–45 (2007).
207. L. Li, X. Wang, and H. Zhai, "Single-shot diagnostic for the three-dimensional field distribution of a terahertz pulse based on pulsed digital holography," *Opt. Lett.* **36**, 2737–2739 (2011).
208. J. Wang, J. Zhao, J. Di, and B. Jiang, "A scheme for recording a fast process at nanosecond scale by using digital holographic interferometry with continuous wave laser," *Opt. Laser Eng.* **67**, 17–21 (2015).
209. S. Suzuki, Y. Nozaki, and H. Kimura, "High-speed holographic microscopy for fast-propagating cracks in transparent materials," *Appl. Opt.* **36**, 7224–7233 (1997).
210. N. Karasawa, "Chirped pulse digital holography for measuring the sequence of ultrafast optical wavefronts," *Opt. Commun.* **413**, 19–23 (2018).
211. N. Karasawa and A. Hirayama, "Experimental demonstration of single-shot chirped pulse digital holography," *Opt. Commun.* **447**, 42–45 (2019).
212. Z. J. Cheng, Y. Yang, H. Y. Huang, Q. Y. Yue, and C. S. Guo, "Single-shot quantitative birefringence microscopy for imaging birefringence parameters," *Opt. Lett.* **44**, 3018–3021 (2019).

213. X. Liu, B. Y. Wang, and C. S. Guo, "One-step Jones matrix polarization holography for extraction of spatially resolved Jones matrix of polarization-sensitive materials," *Opt. Lett.* **39**, 6170–6173 (2014).
214. Y. Kim, J. Jeong, J. Jang, M. W. Kim, and Y. Park, "Polarization holographic microscopy for extracting spatio-temporally resolved Jones matrix," *Opt. Express* **20**, 9948–9955 (2012).
215. M. M. Sreelal, R. V. Vinu, and R. K. Singh, "Jones matrix microscopy from a single-shot intensity measurement," *Opt. Lett.* **42**, 5194–5197 (2017).
216. X. Liu, Y. Yang, L. Han, and C. Guo, "Fiber-based lensless polarization holography for measuring Jones matrix parameters of polarization-sensitive materials," *Opt. Express* **25**, 7288–7299 (2017).
217. Y. Ohtsuka and K. Oka, "Contour mapping of the spatiotemporal state of polarization of light," *Appl. Opt.* **33**, 2633–2636 (1994).
218. D. Beghuin, E. Cuhe, P. Dahlgren, C. Depeursinge, G. Delacretaz, and R. P. Salathé, "Single acquisition polarisation imaging with digital holography," *Electron. Lett.* **35**, 2053–2055 (1999).
219. T. Colomb, P. Dahlgren, D. Beghuin, E. Cuhe, P. Marquet, and C. Depeursinge, "Polarization imaging by use of digital holography," *Appl. Opt.* **41**, 27–37 (2002).
220. T. Colomb, F. Dürr, E. Cuhe, P. Marquet, H. G. Limberger, R.-P. Salathé, and C. Depeursinge, "Polarization microscopy by use of digital holography: application to optical-fiber birefringence measurements," *Appl. Opt.* **44**, 4461–4469 (2005).
221. P. Girshovitz and N. T. Shaked, "Real-time quantitative phase reconstruction in off-axis digital holography using multiplexing," *Opt. Lett.* **39**, 2262–2265 (2014).
222. B. Sha, X. Liu, X. L. Ge, and C. S. Guo, "Fast reconstruction of off-axis digital holograms based on digital spatial multiplexing," *Opt. Express* **22**, 23066–23072 (2014).
223. P. Girshovitz and N. T. Shaked, "Fast phase processing in off-axis holography using multiplexing with complex encoding and live-cell fluctuation map calculation in real-time," *Opt. Express* **23**, 8773–8787 (2015).
224. B. Sha, Y. Lu, Y. Xie, Q. Yue, and C. Guo, "Fast reconstruction of multiple off-axis holograms based on a combination of complex encoding and digital spatial multiplexing," *Chin. Opt. Lett.* **14**, 60902 (2016).
225. A. V. Zea, J. F. Barrera, and R. Torroba, "Cross-talk free selective reconstruction of individual objects from multiplexed optical field data," *Opt. Laser Eng.* **100**, 90–97 (2018).
226. M. Paturzo, P. Memmolo, L. Miccio, A. Finizio, P. Ferraro, A. Tulino, and B. Javidi, "Numerical multiplexing and demultiplexing of digital holographic information for remote reconstruction in amplitude and phase," *Opt. Lett.* **33**, 2629–2631 (2008).
227. C. Rosales-Guzmán, N. Bhebhe, N. Mahonisi, and A. Forbes, "Multiplexing 200 spatial modes with a single hologram," *J. Opt.* **19**, 113501 (2017).
228. T. Tahara, T. Akamatsu, Y. Arai, T. Shimobaba, T. Ito, and T. Kakue, "Algorithm for extracting multiple object waves without Fourier transform from a single image recorded by spatial frequency-division multiplexing and its application to digital holography," *Opt. Commun.* **402**, 462–467 (2017).
229. T. Tahara, T. Gotohda, T. Akamatsu, Y. Arai, T. Shimobaba, T. Ito, and T. Kakue, "High-speed image-reconstruction algorithm for a spatially multiplexed image and application to digital holography," *Opt. Lett.* **43**, 2937–2940 (2018).

230. A. Mahjoubfar, C. Chen, K. R. Niazi, S. Rabizadeh, and B. Jalali, "Label-free high-throughput cell screening in flow," *Biomed. Opt. Express* **4**, 1618–1625 (2013).
231. F. Merola, P. Memmolo, L. Miccio, R. Savoia, M. Mugnano, A. Fontana, G. D'Ippolito, A. Sardo, A. Iolascon, A. Gambale, and P. Ferraro, "Tomographic flow cytometry by digital holography," *Light Sci. Appl.* **6**, e16241 (2017).
232. G. Dardikman, Y. N. Nygate, I. Barnea, N. A. Turko, G. Singh, B. Javidi, and N. T. Shaked, "Integral refractive index imaging of flowing cell nuclei using quantitative phase microscopy combined with fluorescence microscopy," *Biomed. Opt. Express* **9**, 1177–1189 (2018).
233. V. Bianco, P. Memmolo, P. Carcagnì, F. Merola, M. Paturzo, C. Distante, and P. Ferraro, "Microplastic identification via holographic imaging and machine learning," *Adv. Intell. Syst.* **2**, 1900153 (2020).
234. C. Edwards, A. Arbabi, G. Popescu, and L. L. Goddard, "Optically monitoring and controlling nanoscale topography during semiconductor etching," *Light Sci. Appl.* **1**, e30 (2012).
235. M. Lucente, "Computational holographic bandwidth compression," *IBM Syst. J.* **35**, 349–365 (1996).
236. P. Memmolo, M. Paturzo, A. Pelagotti, A. Finizio, P. Ferraro, and B. Javidi, "Compression of digital holograms via adaptive-sparse representation," *Opt. Lett.* **35**, 3883–3885 (2010).
237. P. A. Cheremkhin and E. A. Kurbatova, "Wavelet compression of off-axis digital holograms using real/imaginary and amplitude/phase parts," *Sci. Rep.* **9**, 7561 (2019).
238. T. J. Naughton, Y. Frauel, B. Javidi, and E. Tajahuerce, "Compression of digital holograms for three-dimensional object reconstruction and recognition," *Appl. Opt.* **41**, 4124–4132 (2002).
239. A. E. Shortt, T. J. Naughton, and B. Javidi, "Compression of digital holograms of three-dimensional objects using wavelets," *Opt. Express* **14**, 2625–2630 (2006).
240. F. Dufaux, Y. Xing, B. Pesquet-Popescu, and P. Schelkens, "Compression of digital holographic data: an overview," *Proc. SPIE* **9599**, 95990I (2015).
241. E. A. Kurbatova, P. A. Cheremkhin, N. N. Evtikhiev, V. V. Krasnov, and S. N. Starikov, "Methods of compression of digital holograms," *Phys. Procedia* **73**, 328–332 (2015).
242. K. Jaferzadeh, S. Gholami, and I. Moon, "Lossless and lossy compression of quantitative phase images of red blood cells obtained by digital holographic imaging," *Appl. Opt.* **55**, 10409–10416 (2016).
243. G. Barbastathis, A. Ozcan, and G. Situ, "On the use of deep learning for computational imaging," *Optica* **6**, 921–943 (2019).
244. H. Ren, W. Shao, Y. Li, F. Salim, and M. Gu, "Three-dimensional vectorial holography based on machine learning inverse design," *Sci. Adv.* **6**, eaaz4261 (2020).



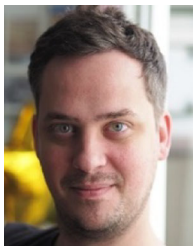
Natan T. Shaked is a Full Professor in the Department of Biomedical Engineering at Tel Aviv University, Israel, and the director of the Biomedical Optical Microscopy, Nanoscopy and Interferometry (OMNI) Research Group. In 2011, Prof. Shaked was a Visiting Assistant Professor in the Department of Biomedical Engineering at Duke University, Durham, North Carolina, USA. Shaked received his B.Sc., M.Sc., and Ph.D. degrees in Electrical and Computer Engineering from Ben-Gurion

University of the Negev, Israel, in 2002, 2004, and 2008, respectively. Prof. Shaked is the coauthor of more than 80 refereed journal papers and more than 150 conference

papers. His research focuses on label-free biomedical imaging and digital holography. He is chairing the SPIE Label-Free Imaging and Sensing (LBIS) annual conference in SPIE Photonics West, and heading the IEEE Israeli Chapter on Engineering in Medicine and Biology.



Vicente Micó is an Associate Professor at the Universitat de Valencia, Spain, and a member of the Optoelectronic Image Processing Group headed by Prof. Javier García. He received a Ph.D. in Optics in 2008, an M.S. in Physics in 2000, and a BS in Optics and Optometry in 1999. He is actively working on optical metrology, including vibration and deformation metrology, digital holography, optical super-resolution, speckle applications, and lensless coherent imaging. Prof. Mico has founded Cytolovu SL, a start-up company focusing on quantitative phase microscopy. As an optometrist, he is working on theoretical aspects of physiological and visual optics, as well as on developing novel optometric instruments for the measurement of ocular parameters. He has coauthored approximately 100 peer-reviewed papers, 40 of them on super-resolution in coherent optical microscopy.



Maciej Trusiak is an Assistant Professor at the Institute of Micromechanics and Photonics Warsaw University of Technology. He received his B.Sc., M.Sc., and Ph.D. in Photonics Engineering from the Warsaw University of Technology in 2011, 2012, and 2019, respectively. He then conducted a year-long postdoctoral research in the Optoelectronic Image Processing Group headed by Prof. Javier García in the University of Valencia, Spain. He is actively working in computational imaging, optical metrology, interferometry, quantitative phase microscopy, lensless coherent imaging, and fringe pattern analysis. He is a coauthor of more than 60 peer-reviewed journal papers.



Arkadiusz Kuś is an Assistant Professor in the Institute of Micromechanics and Photonics, Warsaw University of Technology, Poland. He received his M.Sc. and Ph.D. in automation and robotics with specialization in photonics engineering from Warsaw University of Technology, Faculty of Mechatronics in 2012 and 2017, respectively. His current research interests include optical diffraction tomography, digital holographic microscopy, and optical design.



Simcha K. Mirsky is a Ph.D. student in Shaked's group in the Department of Biomedical Engineering at Tel Aviv University, Israel. He received his BSc. in Medical Engineering from the Jerusalem College of Technology in 2012. After his B.Sc., he completed his army service in the Medical Engineering Branch of the Israeli Defense Forces as an officer in the Medical Engineering Development Unit. He received his M.Sc. in the Department of Biomedical Engineering at Tel Aviv University in 2018.